이학박사 학위논문

Biophysical Studies on the Neurobiological Phenomena Related to Learning and Memory Using the Combined AFM and CLSM

원자간 힘 현미경-공초점 레이저 주사 현미경
통합기기를 이용한, 학습 및 기억 관련
신경생물학적 현상에 관한 생물리학적 연구

2013 년 8 월

서울대학교 대학원
화학부 물리화학
박 애 영

Thesis for the Degree of Doctor

Biophysical Studies on the Neurobiological Phenomena Related to Learning and Memory Using the Combined AFM and CLSM

by

Aee-Young Park

Supervisor: Prof. Seonghoon Lee

Department of Chemistry

Graduate School

Seoul National University

August 2013

Abstract

This thesis research focuses on the development of the combined atomic force microscopy and confocal laser scanning microscopy (AFM-CLSM) system and its application to understanding learning and memory. The developed combined AFM-CLSM system is an efficient and suitable method to study the fine 3D structural changes in live cells and the relationship between morphological/structural changes and intracellular functional changes such as the dynamic change of synaptic connections related to neuronal mechanism or phenomena.

Brain-derived neurotrophic factor (BDNF) is a major regulating neurotrophin of synaptic transmission and plasticity at adult synapses in many regions of the central nervous system (CNS). The diverse functions of BDNF are mediated by their specific interaction with tyrosin kinase B (TrkB) receptors. We have utilized a quantum dot (QD)-based immunocytochemistry technique to detect TrkB receptor proteins. We applied the combined AFM-CLSM system to detect accurate localization of endogenous TrkB receptor proteins, which are targeted to the surface membrane for the function in mouse hippocampal neurons. We found that endogenous TrkB receptor proteins are distributed in a highly diffuse manner in the central soma, discrete in the neurites. This result shows that the combined AFM-CLSM system is highly efficient for discovering precise correlation between localization of immunocytochemically labeled specific proteins and cellular structures in a three-dimensional manner.

Structural and functional plasticity of *Aplysia* mechanosensory presynaptic neurons has been investigated to understand the mechanism of learning and memory. Long-term

facilitation, a well-known cellular model for long-term memory in *Aplysia*, is known to be accompanied by new synaptic growth. We applied the combined AFM-CLSM system to image accurate and volumetric changes in presynaptic structure (varicosities) of live *Aplysia* neurons. We found that preexisting varicosities filled with synaptic vesicles showed a volumetric increase following a continuous (massed) application of serotonin (5-hydroxytriptamine, 5-HT) in conjunction with an increase in the total number of varicosities. This volumetric change in synaptic structure improves strength of the synaptic connection and efficiency of the synaptic transmission due to an increase in active zones of synaptic areas and synaptic vesicle pools of synaptic varicosities.

This result shows that the combined AFM-CLSM system is highly efficient for measuring accurate and detailed structural changes together with the functional changes in synaptic contacts of live neurons.

Keywords: Atomic force microscopy (AFM), Confocal laser scanning microscopy (CLSM), TrkB receptor, synaptic plasticity, long-term facilitation (LTF), varicosity, *Aplysia*

Student Number: 2003-30867

Table of Contents

Appendix

List of Schemes

List of Figures

List of Abbreviations

5-HT	5-hydroxytriptamine
AFM	Atomic force microscopy
BDNF	brain-derived neurotrophic factor
CLSM	Confocal laser scanning microscopy
CNS	central nervous system
DIC	differential interference contrast
DLS	dynamic light scattering
EGFP	enhanced green fluorescence protein
EM	electron microscope
FRET	fluorescence resonance energy transfer
LTD	long-term depression
LTF	long-term facilitation
LTP	long-term potentiation
MPA	mercaptopropionic acid
NTV	neutravidin
NT	neurotrophin
OA	oleic acid
OM	optical microscopy
QD	quantum dot
SEM	scanning electron microscopy
TEM	transmission electron microscopy
Trks	tyrosine kinase receptors

Chapter I.

Introduction

1.1 Motivation

For many years, a major focus of neuroscience research has been to understand the cellular changes that occur during learning and memory acquisition. Learning is defined as the process of acquiring new information or skills, whereas memory refers to the persistence of learning that can be revealed at a later time (*1*). Memory is the usual consequence of learning and reflects the enduring changes in the nervous system that result from transient experiences (*2*). Synaptic plasticity refers to the changes in the strength of synaptic function, and this process is currently a major focus of research on the neurobiology of learning and memory (*3-5*). Memory can be grouped into at least two general categories: explicit and implicit memory (*6*). Explicit or declarative memory is the conscious recall of knowledge about people, places, and things, and it is particularly well developed in the vertebrate brain. Implicit or nondeclarative memory is memory for motor skills and other tasks and is expressed through performance, without conscious recall of past experience; it includes simple associative forms, such as classical conditioning, and nonassociative forms, such as sensitization and habituation. Explicit memory is critically dependent on structures in the medial temporal lobe of the cerebral cortex, including the hippocampal formation. Implicit memory involves the cerebellum, the striatum, the amygdale, and in the simplest cases, the sensory and motor pathways recruited for particular perceptual or motor skills utilized during the learning process. As a result, implicit memory can also be studied in a variety of simple reflex systems, including those of higher invertebrates, whereas explicit forms can best be studied in mammals. For both implicit and explicit memory, synaptic plasticity includes two types of memory; short-term changes in the strength or efficacy of

neurotransmission and longer-term changes in the structure and number of synapses (*7*). This long-term process occurring in explicit memory is called long-term potentiation (LTP), whereas that occurring in implicit memory is called long-term facilitation (LTF).

Long-term potentiation (LTP) has been studied as one of the major mechanisms of learning and memory in the vertebrate brain. The hippocampus is best recognized for its role in declarative memory and spatial learning (*8*). Neurotrophins are a family of growth factors regulating differentiation, maturity, and survival of neurons. The diverse functions of neurotrophins are mediated by their specific interaction with tyrosine kinase receptors (Trks) (*9*). The Trks include TrkA (a receptor for nerve growth factor (NGF)), TrkB (a receptor for brain-derived neurotrophic factor (BDNF), neurotrophin-4/5 (NT-4/5)), and TrkC (a receptor for neurotrophin-3 (NT3)). Lohof et al. was the first to show neurotrophin-evoked increases in synaptic transmission (*10*). Specially, BDNF has emerged as a major regulator of synaptic transmission and plasticity at adult synapses in many regions of the central nervous system (CNS). Due to this unique role of BDNF, of all the neurotrophins, BDNF/TrkB (Tyrosine Kinase B) is the only signaling system exhibiting widespread distribution across the subregions of the hippocampus and the adult forebrain (*11*). The binding of BDNF to TrkB receptor activates down-stream intracellular cascades, regulating neuronal development and plasticity, long-term potentiation (LTP) (*12-13*). Application of BDNF for several minutes can trigger a long-lasting increase in synaptic efficiency dubbed BDNF-induced LTP (*12, 14*). Additionally, genetic ablation of TrkB gene in the forebrain changes hippocampal spine density and length in an age- and region-specific manner, which in turn may affect synaptic transmission and plasticity. To understand the pathogenic mechanism related to the BDNF/TrkB signaling as well as the development and

regulation of the nervous system, it is important to monitor the localization of endogenous TrkB receptors on hippocampal neurons.

Long-term facilitation (LTF), which has been studied as one of the major mechanisms of learning and memory in *Aplysia* nervous system, is accompanied by functional and structural changes in the synapses between sensory and motor neurons (*15-18*). Long-term treatment of serotonin (5-hydroxytriptamine, 5-HT) induces LTF, and the long-term increase in synaptic strength following the induction of LTF is maintained by structural changes such as the growth of new synaptic connections (varicosities) (*15, 19*). Therefore, this long-term increase in synaptic strength is observed by an increase in the number of synaptic connections (*20-21*). Additionally, it has been further observed with the course of time that the preexisting empty varicosities were rapidly activated by filling with synaptic vesicles and newly formed synaptic varicosities, most of which were filled with synaptic vesicles, were slowly generated (*16*). All the observations suggest the idea that synaptic facilitation can be supported by increase in the number of functional varicosities filled with synaptic vesicles. However, the preexisting varicosities filled with synaptic vesicles were considered relatively stable as they are always present at the fixed location throughout the induction and maintenance of LTF (*22*). Previous studies on LTF are more focused on the numerical increase in functional varicosities but not volumetric increase in them due to the limitations in possible imaging techniques for a three-dimensional (3D) real-time measurement of the morphological changes in preexisting functional varicosities. Thus, quantitative analyses of the fine 3D structural changes in the same preexisting synaptic varicosities during LTF are strongly required. Additionally, parallel analyses on the structural changes in synaptic varicosities and the localization of synaptic vesicles

within the same varicosities are required to investigate the relationship between structural changes and functional changes during LTF.

Thus, a novel tool, which is highly efficient for measuring accurate and detailed dynamic structural changes together with the functional changes of synaptic structures of live neurons, is required to study time-resolved functional and structural changes of synaptic connections. Thus, we have developed the combined AFM and CLSM (AFM-CLSM) instrument and applied to discovering the precise localization of endogenous TrkB receptors by correlating the fluorescent image with nanometer-scale cellular structures resolved by AFM and investigating structural changes in synaptic connections in response to LTF-inducing stimuli within live *Aplysia* cultured neurons in addition to acquiring the three-dimensional optical images.

1.2 Introduction to Light Microscopy

1.2.1 Light microscopy

The light microscope can be used to visualize objects as small as 200 nanometers (nm) in diameter, which enables the investigation of animal cells that typically range between 10 – 100 μm in diameter. In light microscope, light is passed through the specimen and magnified after the light passes through two lenses, an objective lens and an ocular lens (eyepiece). In light microscopy, the crucial issue when viewing samples is not the magnification, but the resolving power of the microscope. This resolving power refers to the ability of the microscope to distinguish two separate features that are

in close proximity to each other. As mentioned above, the maximum resolving power of a light microscope is 200 nm and this is limited by the wavelength of the illumination. Although a resolving power of 200 nm is good enough to resolve some of the light subcellular structures, such as the nucleus, it does not enable visualization of the smaller features within the cell or on the cellular surface, such as the cytoskeletal filaments and microvilli. When smaller features need to be visualized other forms of microscopy can be used and these include electron microscopy, fluorescence microscopy and atomic force microscopy.

1.2.2 Fluorescence microscopy

Fluorescence microscopy can be applied to the molecules which must first be labeled with fluorescent dyes. Fluorescent dyes can be used in either fixed or living cells. When the fluorescence molecules are excited by a particular wavelength of light, they emit at a second wavelength which can be visualized by using the appropriate filter set that only transmits the emitted light through to the eyepiece or camera attached to the microscope. The emission of this light usually occurs after a very short period (approximately 10^{-8} seconds) and is always produced at a longer wavelength than the absorbed light according to the Stokes shift, which results from a small dissipation of the energy during the excitation state (*23*).

Since it came to prominence, fluorescence microscopy has been used to study a variety of molecules and processes within cells and has contributed enormously to the field of cell biology. Some of the most important recent advances in fluorescence microscopy include the use of antibodies labeled with a fluorescence probe, which is

directed against a specific protein such as actin. However, fluorescence microscopy has major limitation. That is, the out-of-focus parts of a thick specimen give rise to a uniform glow, making it very difficult to distinguish fine structures (*24*). As a consequence scientists began to investigate a new type of microscope, the confocal microscope, which is now widely used in biological research.

1.2.3 Confocal Laser Scanning Microscopy (CLSM)

The confocal scanning optical microscope (CSOM) was first invented in 1955 by Marvin Minsky (*23*). The application of confocal microscopy deeply improved the image resolution compared to conventional microscopes, but the most profound advantage of confocal microscopy is its ability to discriminate wanted information (in focus) from unwanted signal that is out-of-focus for imaging purposes and 3D measurements.

The basic principle of this microscope is illustrated in Fig 1.1. In confocal microscopy only one spot on the sample is illuminated at a time through a pinhole, in contrast with conventional wide field microscopy where the whole sample is illuminated and imaged at once. The light scattered by the specimen is collected through the same or another pinhole. By scanning the spot or the sample in a raster pattern a complete image can be formed. Scattered light from an out-of-focus spot will be de-focused on the pinhole and hence will not pass to the detector. Confocal microscopy therefore enables three-dimensional optical sectioning.

In the early years the potential of the confocal microscope was not fully developed because of the lack of an adequate light source. The invention of the laser solved this

problem and in 1969 Davidovits & Egger developed a CSOM using a laser as a light source (*25*). In 1979, Brakenhoff and co-workers demonstrated a well engineered confocal laser scanning microscope, showing the improvement in definition and contrast obtainable with confocal imaging and its use in biological applications (*26*).

CLSM enables 3D reconstruction of whole, or parts of a specimen, by taking a series of optical slices through the specimen and using computer software to reconstruct the images. Image analysis software is also available which helps analyze images and cellular processes. Also new advances, such as tools that enable studies of fluorescence resonance energy transfer (FRET) and fluorescence lifetime imaging, are becoming more widely used to help study and visualize cellular processes and molecular interactions within cells as never before (*23, 27*). However, optical microscopy detects only fluorescence-tagged molecules, showing limitations in achieving the information of the real three-dimensional cellular structure due to the variations in the amount of gene expression between the neurons and the instability of loaded organic dyes within the cell during imaging process. Additionally, the lateral and axial resolution of optical microscopy is limited by the diffraction to about half the wavelength of the light used, thus restricting acquirement of high-resolution structural image.

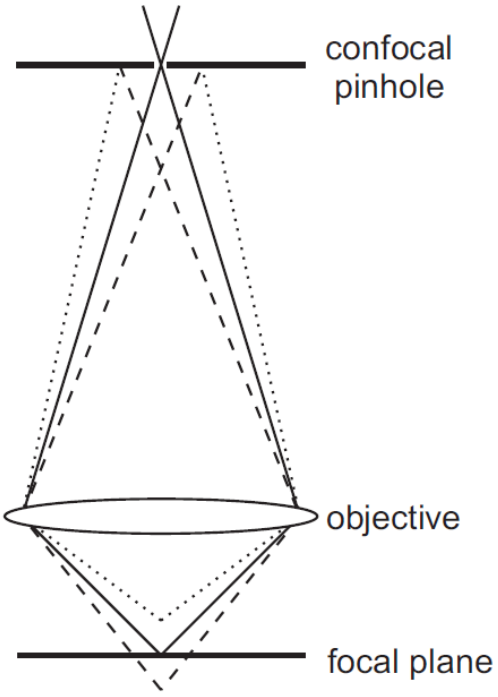

Figure 1.1 Basic principle of the confocal microscope. Light from the focal spot passes the confocal pinhole and will be detected (solid line). Out-of-focus light will be blocked by the pinhole (dashed and dotted lines).

1.3 Introduction to Electron Microscopy

The electron microscope (EM) was developed in the 1930's by Ernst Ruska and first used to study biological specimens by Albert Claude, Keith Porter and George Palade (*28*). The resolution of the electron microscope is much greater than that of the light microscope because it uses an electron beam to illuminate the specimen and this beam has an effective wavelength typically 100,000 times shorter than that of visible light (*29*). This gives a theoretical resolution of 0.002 nm which, because of the design of the magnetic coils of the microscope, is not practically possible. This is due to distortion produced by the magnetic coils when a small angle of illumination is used. Thus the realistic resolving power of the best electron microscopes is about 0.2nm (*28*).

There are two types of electron microscopy which can be used to study biological samples such as cells, these being scanning electron microscopy (SEM) and transmission electron microscopy (TEM). With both techniques, samples need to be processed in such a way that they become fixed (dead) and this is usually a time consuming process. Also, once processed for EM studies biological samples such as cells may no longer provide a true representative compared with an unprocessed sample.

In TEM the samples are usually sliced into thin sections (50-100nm), which enables the observation of subcellular structures. After being fixed and stained using metallic compounds, the sample is usually embedded in a plastic resin and sliced, ready for visualization of the sample. In TEM images are obtained as the electrons pass through the specimen with the metallic stain acting as an opaque layer for the electrons (*29*).

In contrast SEM is a technique which enables visualization of the surface of

biological specimens such as cells. In SEM the sample is fixed or freeze-dried, in order to preserve the shape. The sample is then coated with a heavy metal, usually gold and viewed directly with the microscope. During SEM the electron beam is scanned back and forth across the sample. As the beam scans the sample the electrons are deflected from the surface and secondary electrons are induced and emitted which are detected by a photomultiplier which is used to form a 3D image of the sample (*29*).

1.4 Introduction to Atomic Force Microscopy (AFM)

1.4.1 Principle of operation

Since its invention in 1986 (*30*), the atomic force microscope (AFM) has become an important tool in many areas of research and the last decade in particular has witnessed a large and diverse range of studies in the biological sciences (*31-37*). The standard layout of an AFM is shown in Figure 1.2. The main components of an AFM consist of the AFM probe (a sharp tip mounted on a soft cantilever), the optical lever that allows for measuring the cantilever deflections, the feedback loop that allows for monitoring the interaction forces between the molecules on the tip with the ones on the cell surface, the piezoelectric scanner that moves the tip in respect with the sample in a 3D pattern, and a conversion system from raw data acquired by the instrument into an image or other useful display.

The purpose of an AFM is to characterize a sample by bringing a sharp probe in close proximity to the sample surface. The probe tip is affected by the forces on the surface, some attractive and some repulsive (*38-39*). These forces cause a deflection of

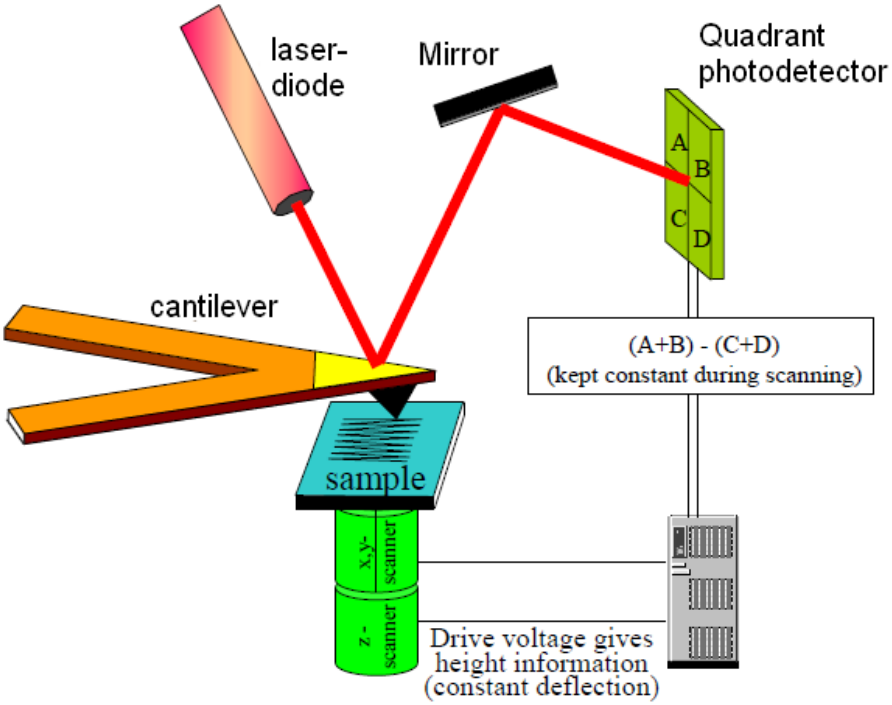

Figure 1.2 Schematic diagram of AFM: showing the main components of the AFM

the cantilever on which the tip resides and this deflection is detected. In principle, the cantilever deflection follows Hooke's law of the displacement *d* of a spring from equilibrium

$$F = -k \cdot d,$$

where *k* is the spring constant and *F* is the force applied. The spring constant *k* is a measure of the stiffness of the cantilever and approximated by

$$k = \frac{Y \cdot b \cdot h^3}{4 \cdot l^4},$$

where *Y* is Young's modulus, *b* is the width, *h* the height and *l* the length of the cantilever. Young's modulus describes the ratio of stress to strain.

An optical lever method has been used to detect the cantilever deflection, in which a laser beam is bounced off of the cantilever and back onto a split photo detector (*40*). Typical photo detectors for common AFMs have four quadrants, allowing both the longitudinal bending modes and lateral torsional modes of the cantilever to be detected. The sensitivity of such a system is in the range of 0.1 nm (*41*). The most sensitive part of an AFM is the tip that interacts directly with the sample surface. The most common probes are constructed from silicon or silicon nitride using microfabrication techniques. The properties and dimensions of the cantilever and tip play a major role in determining the sensitivity and resolution of the AFM (*42*). The AFM tip must be chosen carefully depending on the specific application. In general, the cantilever should be soft enough to be deflected at very small forces, and the tip radius should be comparable with the features of interest. The AFM scanners are made from piezoelectric material, which expands or contracts proportionally with an applied voltage. The piezoelectric scanner can move very precisely with very good reproducibility for small displacements, but for displacements > 70 % of the full-scale displacement, the piezoelectric response is

nonlinear. The commercially available AFM featuring closed-loop feedback systems independently monitors the scanner movement and correct its motion for nonlinearity. There are two types of scanner configurations: scanned tip AFM (where the piezoelectric scanner is rigidly attached to the probe and is moved over the sample surface, which stands still) and scanned sample AFM (where the scanner is attached to the sample and is moved under the tip).

1.4.2 Operation modes of AFM

Interactions between sample and AFM probe tip are characterized by repulsive short range and attractive long range force, with a zero interaction force at a fraction of a nanometer (Figure 1.3). The long range forces are weak attractive van der Waals forces that are present until the separation distance becomes so small that the electron clouds begin to repel each other electrostatically. From that distance and closer, short range forces between the sample and tip atoms start to repulse each other. Both types of forces can be used for topographical measurement: short range forces for contact mode, and long range forces for intermittent contact mode.

Contact mode

In Contact mode imaging, the AFM tip is brought in contact with the sample and set to scan the sample in a *xy* raster pattern. The feedback loop maintains a constant deflection (force) of cantilever with respect to the sample surface by moving the *z* scanner for each *xy* coordinate. This change in *z* axis corresponds to the topographical height of the sample at each given point. The height image preserves the true

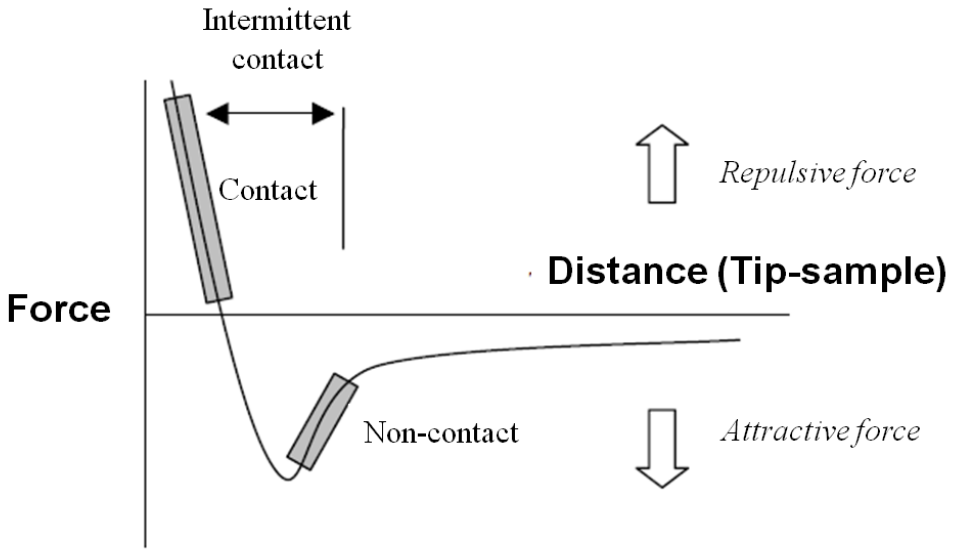

Figure 1.3 Schematic diagram of van der Waals force versus distance between the tip and the surface

topographical height information of the sample. Also, a “deflection” image is captured by recording any deviation from the set-point deflection value of the cantilever. This type of imaging loses the true height information, but it presents more fine details of the sample than the height image because the feedback loop response is faster for correcting the position of the small cantilever, in comparison with correcting the position of the piezoelectric element.

Intermittent Contact mode (tapping mode or AC mode)

For very soft samples, contact mode might not be the best choice due to the friction between the AFM tip and the sample surface. In Tapping mode, the cantilever vibrates at its resonant frequency (bounces up and down) under an external electrical excitation. While rastering the sample in *xy* the AFM tip briefly touches the sample at the bottom of each swing, producing a decrease in the oscillation amplitude. Similar to the constant force in contact mode, the feedback loop keeps this decrease in oscillation amplitude at a constant value by moving the piezoelectric tube, and a height image can be recorded. Instead of deflection images, amplitude images are captured as the tip scans the sample. Any deviations from the set-point amplitude value of the oscillating cantilever are recorded and the image is constructed.

1.4.3 AFM applications specific to biology

AFM is not a conventional microscope that collects and focuses light. The most characteristic property of the AFM is that the images are acquired by “feeling” the sample surface without using light. Thus, not only the sample topography can be

recorded with atomic resolution, but also material characteristics and the eventual strength of the interaction between the sample surface and the AFM tip. Due to the fact that no light is involved in acquiring the sample properties, the resolution achieved by the AFM is not limited by the wavelength of the radiation that investigates the sample, as in classical light microscopy. Thus, the AFM reaches a resolution far below the diffraction limit offered by light microscopy, being limited only by the tip radius and the spring constant of the cantilever.

The advantage of the AFM in imaging in the fluidic environment provides unique opportunity of observing biochemical and physiological process in real time at molecular resolution, which cannot be achieved by other electron-based microscopic techniques, with similar resolution but need to be performed in vacuum. This makes AFM attract more and more attentions from biological communities. Three significant merits make AFM a promising tool in biochemical and microbiological applications. Firstly, native biological molecules and cells can be imaged directly using AFM requiring little or no sample pre-treatment. Secondly, three-dimensional (3D) reconstruction of the sample surface at a resolution similar to Electron microscopy (EM) can be achieved. Thirdly, AFM offers an unprecedented opportunity for imaging biological molecules and cells in their physiological environments and for studying biologically important dynamic processes in real time.

1.5 Combined AFM and CLSM

Traditional AFM imaging is based on very general tip sample interactions, which has been utilized to reveal unprecedented topography of various biosystems with

nanometer scale resolution. However, stand-alone AFM is restricted to correlate structural features with functionality. Several other modes of AFM, such as lateral force microscopy (*43-45*), chemical force microscopy (*46-47*) and phase contrast imaging (*48*) use material specific tip-sample interactions to improve the chemical specificity. However, these modes are also often not distinctive enough to reliably identify surface species.

Optical spectroscopy and imaging, on the other hand, are well established techniques enabling the spectroscopic discrimination of distinct species in the sample. By fluorescent labeling of specific proteins it is possible to follow the processes and dynamics of these components within living cells. Optical parameters such as intensity, wavelength, polarization and fluorescence lifetime provide valuable information about the specimen and its surroundings. In particular, CLSM, which obtains the depth-resolved (z-stacked) fluorescent image by controlling the depth of a focal plane to eliminate out-of-focus light in specimens, has been used to follow three-dimensional dynamics of fluorescently-labeled specific proteins or molecular components within live cells and map intracellular molecular mechanisms (*49*). However, one of the major disadvantages of optical spectroscopy is its comparatively poor spatial resolution.

Remarkably, AFM and CLSM have complementary strengths and weaknesses. Therefore, a combination between AFM and CLSM provides a very powerful tool in biological research. Such a combined AFM and CLSM system directly combines high resolution 3D structural imaging with chemically specific optical imaging applies to dynamic changes in morphological/structure and intracellular function. In addition to the added value of combined imaging, Weiss and Wallace *et al* already described the possibilities of using the AFM tip as a force sensor/manipulator while simultaneously

recording optical responses of the molecules under study (*50-51*). The number of potential applications of a combined AFM – CLSM is numerous.

1.6 Outline of this Thesis

This thesis describes the development of a combined atomic force microscopy and confocal laser scanning microscopy (AFM-CLSM), which is efficient for measuring accurate and detailed structural changes together with the functional changes in subcellular structures in live or fixed neurons. This thesis is divided into four chapters.

First of all, various microscopes are briefly reviewed and the expectations of a combined microscope are discussed in this chapter. In chapter 2, the requirements of the combined AFM and CLSM are discussed and the set-up of the instrument is presented. Performances of the instrument and data analysis are described. In chapter 3, the surface staining of endogenous TrkB receptors on the hippocampal neurons was investigated by utilizing QD-based immunocytochemistry. Precise localization of endogenous TrkB receptors related to the cellular structure are investigated to understand the mechanism of LTP related to the BDNF/TrkB signaling as well as the development and regulation of the nervous system. We found that endogenous TrkB receptor proteins are distributed in a highly diffuse manner in the central soma, discrete in the neurites. In chapter 4, structural and functional changes in presynaptic structure (varicosities) of live *Aplysia* neurons during long-term facilitation (LTF) are investigated to understand the mechanism of learning and memory. We found that preexisting varicosities filled with synaptic vesicles showed a volumetric increase in conjunction with the increase in the total number of varicosities. These results have not been examined due to the limitations

of techniques.

1.7 References

(1) Squire, L. R. (1987) *Memory and Brain*, Oxford University Press, New York.

(2) Atkins, C. M., Selcher, J. C., Petraitis, J. J., Trzaskos, J. M., and Sweatt, J. D. (1998) The MAPK cascade is required for mammalian associative learning. *Nat Neurosci 1*, 602-609.

(3) Malenka, R. C., and Nicoll, R. A. (1999) Neuroscience - Long-term potentiation - A decade of progress? *Science 285*, 1870-1874.

(4) Sweatt, J. D. (2001) The neuronal MAP kinase cascade: a biochemical signal integration system subserving synaptic plasticity and memory. *Journal of Neurochemistry 76*, 1-10.

(5) Kind, P. C., and Neumann, P. E. (2001) Plasticity: downstream of glutamate. *Trends in Neurosciences 24*, 553-555.

(6) Hawkins, R. D., Kandel, E. R., and Bailey, C. H. (2006) Molecular mechanisms of memory storage in Aplysia. *Biol Bull 210*, 174-91.

(7) Kandel, E. R. (2001) Neuroscience - The molecular biology of memory storage: A dialogue between genes and synapses. *Science 294*, 1030-1038.

(8) von Bohlen und Halbach, O., Krause, S., Medina, D., Sciarretta, C., Minichiello, L., and Unsicker, K. (2006) Regional- and age-dependent reduction in trkB receptor expression in the hippocampus is associated with altered spine morphologies. *Biol Psychiatry 59*, 793-800.

(9) Xiong, Z. Q., Zheng, J., Shen, W. H., Lu, T. J., Zhou, Y., Chen, Q., Wang, Z., Xiang, T., Zhu, Y. C., Zhang, C., and Duan, S. M. (2008) Clathrin-dependent endocytosis

is required for TrkB-dependent Akt-mediated neuronal protection and dendritic growth. *Journal of Biological Chemistry 283*, 13280-13288.

(10) Lohof, A. M., Ip, N. Y., and Poo, M. M. (1993) Potentiation of Developing Neuromuscular Synapses by the Neurotrophins Nt-3 and Bdnf. *Nature 363*, 350-353.

(11) Bramham, C. R., and Messaoudi, E. (2005) BDNF function in adult synaptic plasticity: The synaptic consolidation hypothesis. *Prog Neurobiol 76*, 99-125.

(12) Kang, H. J., and Schuman, E. M. (1996) A requirement for local protein synthesis in neurotrophin-induced hippocampal synaptic plasticity. *Science 273*, 1402-1406.

(13) Cheng, Q., and Yeh, H. H. (2003) Brain-derived neurotrophic factor attenuates mouse cerebellar granule cell GABA(A) receptor-mediated responses via postsynaptic mechanisms. *J Physiol-London 548*, 711-721.

(14) Kang, H. J., and Schuman, E. M. (1995) Long-Lasting Neurotrophin-Induced Enhancement of Synaptic Transmission in the Adult Hippocampus. *Science 267*, 1658-1662.

(15) Bailey, C. H., and Kandel, E. R. (1993) Structural changes accompanying memory storage. *Annu Rev Physiol 55*, 397-426.

(16) Kim, J. H., Udo, H., Li, H. L., Youn, T. Y., Chen, M., Kandel, E. R., and Bailey, C. H. (2003) Presynaptic activation of silent synapses and growth of new synapses contribute to intermediate and long-term facilitation in Aplysia. *Neuron 40*, 151-65.

(17) Bailey, C. H., and Kandel, E. R. (2008) Synaptic remodeling, synaptic growth and the storage of long-term memory in Aplysia. *Essence of Memory 169*, 179-198.

(18) Bailey, C. H., Kandel, E. R., and Si, K. (2004) The persistence of long-term memory: a molecular approach to self-sustaining changes in learning-induced

synaptic growth. *Neuron 44*, 49-57.

(19) Hatada, Y., Wu, F., Sun, Z. Y., Schacher, S., and Goldberg, D. J. (2000) Presynaptic morphological changes associated with long-term synaptic facilitation are triggered by actin polymerization at preexisting varicositis. *J Neurosci 20*, RC82.

(20) Bailey, C. H., and Chen, M. (1989) Time Course of Structural-Changes at Identified Sensory Neuron Synapses during Long-Term Sensitization in Aplysia. *Journal of Neuroscience 9*, 1774-1780.

(21) Bailey, C. H., and Chen, M. (1988) Long-term memory in Aplysia modulates the total number of varicosities of single identified sensory neurons. *Proc Natl Acad Sci U S A 85*, 2373-7.

(22) Miniaci, M. C., Kim, J. H., Puthanveettil, S. V., Si, K., Zhu, H., Kandel, E. R., and Bailey, C. H. (2008) Sustained CPEB-dependent local protein synthesis is required to stabilize synaptic growth for persistence of long-term facilitation in Aplysia. *Neuron 59*, 1024-36.

(23) Emptage, N. J. (2001) Fluorescent imaging in living systems. *Curr Opin Pharmacol 1*, 521-5.

(24) Amos, W. B., and White, J. G. (2003) How the Confocal Laser Scanning Microscope entered Biological Research. *Biol Cell 95*, 335-342.

(25) Davidovits, P., and Egger, M. D. (1969) Scanning laser microscope. *Nature 223*, 831.

(26) Brakenhoff, G. J., Blom, P., and Barends, P. (1979) Confocal Scanning Light-Microscopy with High Aperture Immersion Lenses. *J Microsc-Oxford 117*, 219-232.

(27) Huebsch, N. D., and Mooney, D. J. (2007) Fluorescent resonance energy transfer: A tool for probing molecular cell-biomaterial interactions in three dimensions.

Biomaterials 28, 2424-2437.

(28) Cooper, G. M., and Hausman, R. E. (2004) *The cell surface.* , 3rd ed., ASM Press.

(29) Kleinsmith, L. J., and Kish, V. M. (1995) *Principles of cell and molecular biology 2nd ed*, Vol. 2nd ed, HarperCollins, New York.

(30) Binnig, G., Quate, C. F., and Gerber, C. (1986) Atomic Force Microscope. *Physical Review Letters 56*, 930-933.

(31) Barrera, N. P., Herbert, P., Henderson, R. M., Martin, I. L., and Edwardson, J. M. (2005) Atomic force microscopy reveals the stoichiometry and subunit arrangement of 5-HT3 receptors. *Proc Natl Acad Sci U S A 102*, 12595-600.

(32) Hoh, J. H., and Hansma, P. K. (1992) Atomic force microscopy for high-resolution imaging in cell biology. *Trends Cell Biol 2*, 208-13.

(33) Jena, B. P. (2006) Cell secretion machinery: studies using the AFM. *Ultramicroscopy 106*, 663-9.

(34) McNally, H. A., and Borgens, R. B. (2004) Three-dimensional imaging of living and dying neurons with atomic force microscopy. *J Neurocytol 33*, 251-8.

(35) Muller, D. J., Hand, G. M., Engel, A., and Sosinsky, G. E. (2002) Conformational changes in surface structures of isolated connexin 26 gap junctions. *EMBO J 21*, 3598-607.

(36) Ohnesorge, F. M., Horber, J. K., Haberle, W., Czerny, C. P., Smith, D. P., and Binnig, G. (1997) AFM review study on pox viruses and living cells. *Biophys J 73*, 2183-94.

(37) Xiong, Y., Lee, A. C., Suter, D. M., and Lee, G. U. (2009) Topography and nanomechanics of live neuronal growth cones analyzed by atomic force microscopy. *Biophys J 96*, 5060-72.

(38) Sarid, D. (1994) *Scanning force microscopy : with applications to electric, magnetic, and atomic forces Rev. ed*, Vol. Rev. ed, Oxford University Press,

New York.

(39) Israelachvili, J. N. (1991) *Intermolecular and surface forces 2nd ed*, Vol. 2nd ed, Academic Press, London ; Orlando, [Fla].

(40) Alexander, S., Hellemans, L., Marti, O., Schneir, J., Elings, V., Hansma, P. K., Longmire, M., and Gurley, J. (1989) An Atomic-Resolution Atomic-Force Microscope Implemented Using an Optical-Lever. *J Appl Phys 65*, 164-167.

(41) Meyer, G., and Amer, N. M. (1990) Simultaneous Measurement of Lateral and Normal Forces with an Optical-Beam-Deflection Atomic Force Microscope. *Appl Phys Lett 57*, 2089-2091.

(42) Morris, V. J., Kirby, A. R., and Gunning, A. P. (1999) *Atomic force microscopy for biologists*, Imperial College Press ; Distributed by World Scientific Pub., London : Singapore ; River Edge, NJ.

(43) Krotil, H. U., Stifter, T., and Marti, O. (2000) Combined dynamic adhesion and friction measurement with the scanning force microscope. *Appl Phys Lett 77*, 3857-3859.

(44) Mate, C. M., Mcclelland, G. M., Erlandsson, R., and Chiang, S. (1987) Atomic-Scale Friction of a Tungsten Tip on a Graphite Surface. *Physical Review Letters 59*, 1942-1945.

(45) Overney, R. M., Meyer, E., Frommer, J., Guntherodt, H. J., Fujihira, M., Takano, H., and Gotoh, Y. (1994) Force Microscopy Study of Friction and Elastic Compliance of Phase-Separated Organic Thin-Films. *Langmuir 10*, 1281-1286.

(46) Frisbie, C. D., Rozsnyai, L. F., Noy, A., Wrighton, M. S., and Lieber, C. M. (1994) Functional-Group Imaging by Chemical Force Microscopy. *Science 265*, 2071-2074.

(47) McKendry, R., Theoclitou, M. E., Rayment, T., and Abell, C. (1998) Chiral discrimination by chemical force microscopy. *Nature 391*, 566-568.

(48) Noy, A., Sanders, C. H., Vezenov, D. V., Wong, S. S., and Lieber, C. M. (1998) Chemically-sensitive imaging in tapping mode by chemical force microscopy: Relationship between phase lag and adhesion. *Langmuir 14*, 1508-1511.

(49) Pawley, J. B. (1995) *Handbook of biological confocal microscopy*, 2nd ed., Plenum Press, New York.

(50) Weiss, S. (1999) Fluorescence spectroscopy of single biomolecules. *Science 283*, 1676-1683.

(51) Wallace, M. I., Molloy, J. E., and Trentham, D. R. (2003) Combined single-molecule force and fluorescence measurements for biology. *J Biol 2*, 4.

Chapter II.

Development of Combined AFM and CLSM

2.1 Introduction

Optical microscopy (OM) and electron microscopy (EM) have been applied as main methods to study the ultrastructure of neuronal components of neuronal cells and neurobiological phenomena accompanying functional dynamics of cellular components or structural changes in neuronal connections within neuronal cells (*1-5*). Optical microscopy generally provides selective and specific visualization of fluorescent molecules, and renders it possible to monitor dynamic changes in these molecules within live neurons or visualize the overall shape of the neurons over time (*6-7*). However, optical microscopy detects only fluorescence-tagged molecules, showing limitations in achieving the information of the real three-dimensional synaptic structure due to the variations in the amount of gene expression between the neurons and the instability of fluorescent molecules during imaging process. Additionally, the lateral and axial resolution of optical microscopy is limited by the diffraction to about half the wavelength of the light used, thus restricting acquirement of high-resolution structural image. In contrast, EM can resolve the complex and fine structure on nanometer scale resolution and show three-dimensional reconstructions from serial ultrathin sections. Therefore, EM has been applied to study the ultrastructure of synaptic connections and function of synaptic connections by immunohistochemistry (*8-10*). However, since EM can be applied only after the fixation of the cells, time-course observation of structural changes and movement of functional molecules in the live neuron is impossible. Thus, a novel tool, which can be applied to live cells, is strongly required to study time-resolved functional and structural changes in synaptic connections.

Recently, a Atomic force microscopy (AFM), which is a nanometer scale resolution scanning-probe device (*11*), has been utilized to reveal unprecedented topography of various biosystems such as eukaryotic cells and viruses, intracellular

structures such as gap junction, receptors, and vesicles, as well as structural dynamics with nanometer resolution under live cell conditions (*12-19*). However, stand-alone AFM is restricted to correlate structural features with functionality. Confocal laser scanning microscopy (CLSM), which obtains the depth-resolved (z-stacked) fluorescent image by controlling the depth of a focal plane to eliminate out-of-focus light in specimens, has been used to follow three-dimensional dynamics of fluorescently-labeled specific proteins or molecular components within live cells and map intracellular molecular mechanisms (*20*). Thus, various efforts have been made to combine AFM and fluorescent microscopy recently to investigate the high-resolution structural image and functionally specific optical image of biosystem related to biological phenomena (*21-27*). Although several examples of AFM and CLSM combinations have been reported in the literature, only simple superimposition of 2D fluorescent image on 3D topography was tried, and integration of 3D topography of live cell with their corresponding 3D fluorescent signals has not been reported yet (*23, 25*).

2.2 Requirements of the Combined AFM and CLSM

The combined microscope is designed for the study on the neurobiological phenomena in physiological condition. The goal of the microscope is to detect localization of subcellular molecules within the cells and to perform imaging of structural changes and intracellular functional changes in live neurons with the course of time. Because of the significant potential for the application for the application of a combined AFM and CLSM in biophysical research, the set-up should be adaptable for the study of a wide range of systems. Additionally, the program to integrate 3D topography of the cellular structure with their corresponding 3D fluorescent signals is required for accurate analysis. These goals lead to a set of demands for the design of the combined microscope:

▪ The AFM and CLSM should be able to measure on the same sample.

▪ The combined microscope should perform under both air and fluid conditions.

▪ The integration program sould be developed for integration between 3D AFM image and 3D CLSM image on the same neuronal region.

▪ The light from the AFM laser to detect the position of the cantilever should be removed from the detection path of the CLSM, thereby reducing background in the fluorescent image and photo-bleaching.

2.3 Set-up of the Combined AFM and CLSM

2.3.1 Combination between AFM and CLSM instruments

A partially custom-built AFM-CLSM system was assembled so that the AFM head could be accommodated on top of the inverted CLSM microscope (Scheme 2.1). A MFP-3D (atomic force microscope, Asylum Research) was built on an IX 81 inverted microscope (Olympus, Tokyo, Japan) coupled to a Fluoview FV 1000 confocal laser scanning microscope (CLSM; Olympus, Tokyo, Japan) with a stainless steel spacer. The sample stage of CLSM was replaced by the X-Y piezo stage on the base plate of AFM. Thus, the sample can be put on the X-Y piezo stage for the measurement. The spacer provided the space between two instruments preventing a collision between a CLSM part (motorized resolving nosepiece) and an AFM part (base plate), as shown in Figure 2.1. Additionally, the objective lens has to be extending to approach to the bottom of the cover glass of the sample dish on the base plate of AFM, when two microscopes were combined. Therefore, the tube extension of the same height to the height of the spacer was fit into the objective lens, as shown in Figure 2.2. Transmitted illumination column and transmitted light lamp housing for DIC (differential interference contrast)

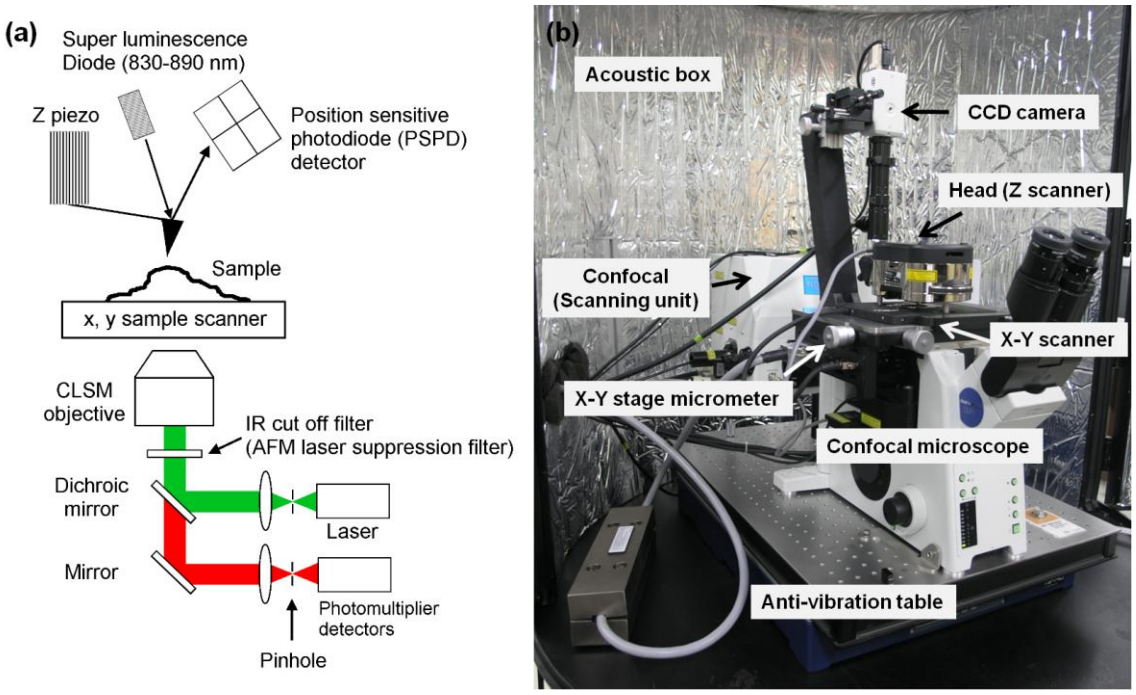

Scheme 2.1 Development of the Combined AFM and CLSM system. (a) Schematic diagram of the combined AFM and CLSM system. (b) Photographic image of the combined AFM and CLSM system.

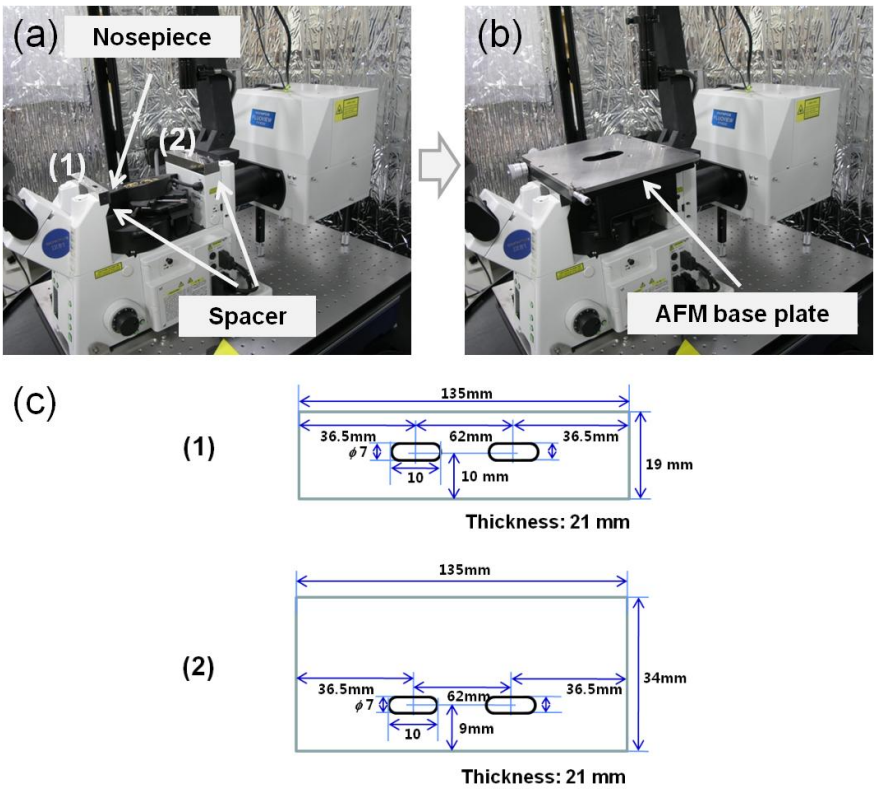

Figure 2.1 How to combine AFM and CLSM. (a) The spacers (1, 2) were put on the CLSM microscope, after bring the CLSM base plate. (b) AFM base plate was put on the spacers, which provided the space between two instruments preventing a collision between a CLSM part (motorized revolving nosepiece) and an AFM part (base plate). (c) Drawing of the spacers (1, 2)

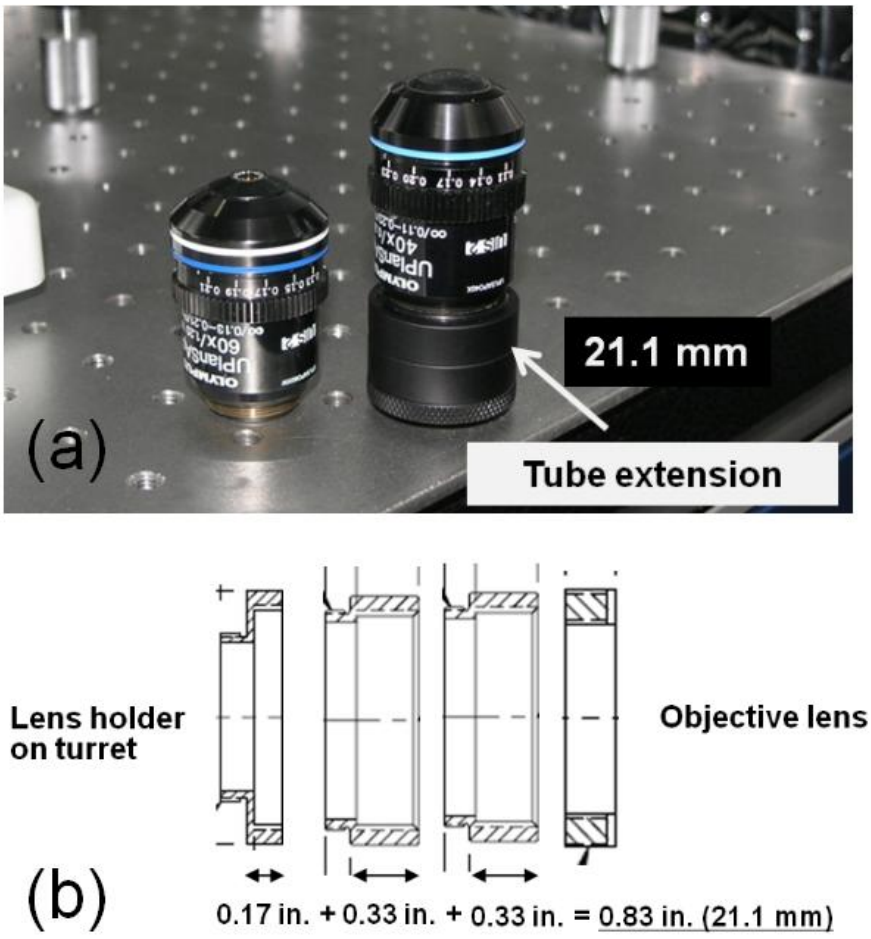

Figure 2.2 Tube extension. (a) Tube extension was fit into the objective lens to let an objective lens approach to the bottom of the cover glass on the X-Y scanner. (b) Assembly of the tube extensions.

observation was removed and replaced by the CCD camera. The combined AFM-CLSM setup was placed on a TS-140 anti-vibration optical table and then the whole instruments were enclosed in an acoustically-isolated chamber.

2.3.2 Fluorescent filters

In combination between AFM and CLSM, the light of IR laser diode, which is used in the AFM head to generate the deflection signal by reflecting in the back of cantilever, passes beside the cantilever and can be collected by the objective and enters the CLSM detector, causing a significant background in the fluorescent image or photo-bleaching of fluorescent molecules within the samples (*28*). Therefore, we inserted an IR cutoff filter with diameter of 25 mm and thickness of 1.1 mm (Edmond, NT53-710), which blocks above 700 nm light, under the objective lens to block the light of AFM laser with a wavelength of 830 - 890 nm.

2.3.3 Preparation of sample dishes

To image the cells with both AFM and CLSM system, cell culture dish was required to be modified specifically. The culture dish was a standard 60 mm Petri dish (BD Falcon) with a 35 mm × 30 mm area drilled from the bottom of the dish. A cover slip with the thickness of 0.13 – 0.16 mm was attached to the bottom of the dish using Sylgard 184 (Dow corning), as shown in Figure 2.3. One crucial requirement to successful imaging is cell attachment to the substrate. There are some cell lines that naturally attach well to glass (cover glasses) or plastic (Petri dishes) which make sample preparation quite easy. However, other cells may require biological adhesives such as poly L-lysine, collagen, laminin or fibronectin. Within this thesis, poly L-lysine coating was applied.

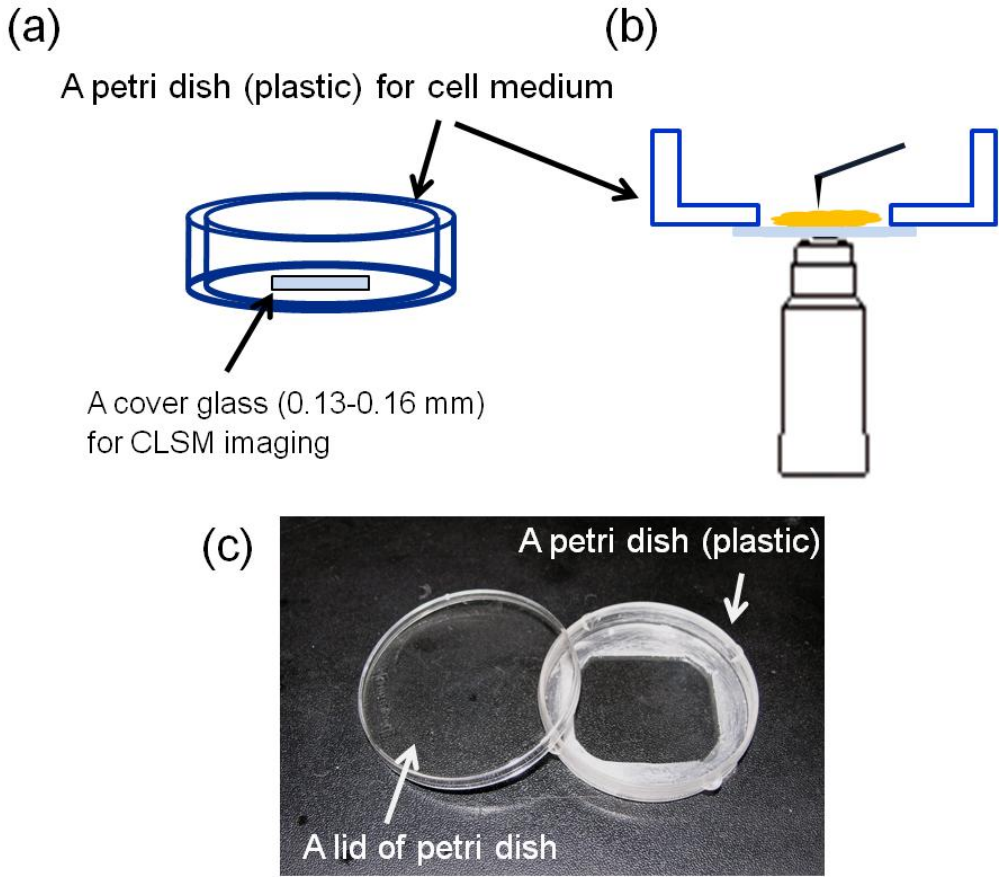

Figure 2.3 Preparation of sample dishes. (a) A standard 60 mm Petri dish (BD Falcon) were drilled from the bottom of the dish with a 35 mm × 30 mm area. A cover slip with the thickness of 0.13 – 0.16 mm was attached to the bottom of the dish using Sylgard 184 (Dow corning). (b) Neuronal cells cultured on the cover slip were imaged with the combined AFM and CLSM. This is not to scale. (C) Photographic image of the culture dish.

2.3.4 Alignment of cantilever tip to optical axis

After putting the sample on the AFM sample stage, we focus a CLSM on the sample and align the cantilever tip to optical axis. The AFM head, on which the cantilever was mounted and laser-aligned, is transferred to the X-Y piezo stage. Due to the relatively small tip dimensions and the limited view of the objectives, a method is needed to find the cantilever tip position, which may initially be far out the viewing field, and align the tip to the sample. The light of xenon lamp related to CCD camera, which is used calibrating the cantilever, passed through the light pathway for transmitted light imaging (DIC) and enters the CLSM transmitted light detector. Thus, we can observe the cantilever and sample within the view of the objective through the eyepieces under xenon lamp on by selecting DIC imaging mode. First of all, we focus a CLSM objective lens on the sample by selecting DIC imaging mode. The second step in the alignment procedure is to adjust the position of the AFM head laterally with the large X-Y stage micrometers, so that the cantilever tip is in the view of the microscope objective. The X-Y micrometer has to adjust between 6 ~ 7 mm from our experience. With selecting fluorescent imaging mode, we can observe both the cantilever and the sample within the view of the objective, as shown in the Figure 2.4. As more and more the cantilever approaches to the surface, the cantilever could be seen clearly, because the surface has been already focused.

2.4 Performance of the Combined AFM and CLSM

2.4.1 Performance of the AFM

In this thesis, AFM analysis is primarily carried out for the study of the cellular

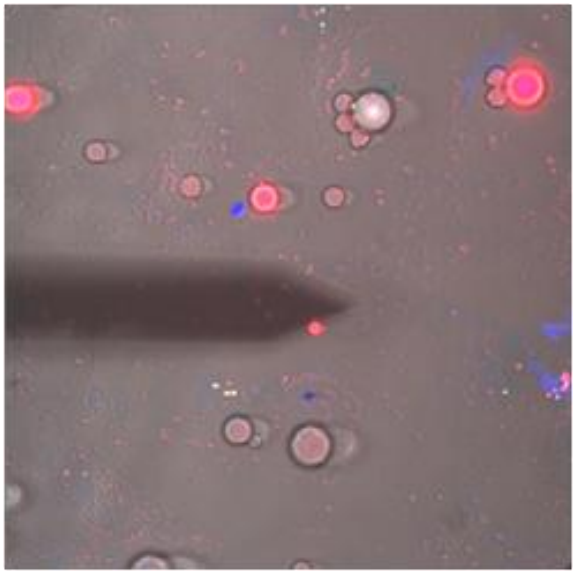

Figure 2.4 Alignment of cantilever tip to optical axis. With selecting fluorescent imaging mode, a transmitted image (from xenon lamp related to CCD camera) and a fluorescent image (red and blue) were displayed together through the eyepieces. This image could not be captured by our system (provided from Asylum research).

morphology under fixed or living conditions in either Contact mode or Tapping mode (also called AC mode). Both techniques can provide useful information on cellular structure. Typically, Tapping mode, which gently taps the surface, reveals features at the cell surface or just below the cell membrane (*29*). Contact mode, on the other hand, applies more pressure onto the surface so that rigid subcellular features such as the cytoskeleton are more suitable to image (*30-31*). Another advantage to Contact mode is that the applied force onto the surface can be calculated after calibrating the cantilever's spring constant. The fixed cell or dried cell is generally measured in Contact mode, whereas the live cell is measured in Tapping mode or low-force Contact mode. Thus, the fixed and dried neuronal cells were imaged in Contact mode in the Chapter 3, whereas the live neuronal cells were imaged in Tapping mode in the Chapter 4.

AFM Contact mode imaging in fluid

Pyrex-nitride cantilevers (spring constant 0.08 N/m, length 200 μm, PNP-TR, NanoWorld) were used for all contact mode imaging. Before imaging, the cantilever was positioned near the cell not to impale the cell structure and left for a further 30 minutes. If imaging is performed in the air, thermal stabilization is not needed. Thermal stability was determined from the sum and deflection meter in the MFP-3D software. Once stable, the deflection optical lever sensitivity (Def OLS) was determined on a bare region of the glass substrate from force versus distance curves taken at 1 Hz (a force curve per second) with the scan size set to 0 μm (no XY tip movement). Figure 2.5 shows the force versus distance curves, this enables the deflection of the cantilever to be recorded by the photodetector in volts, as measured by the displacement (error signal) of the laser spot from its original position (zero deflection) on the detector. This enables plots to be made of deflection (volts) versus z-movement (meters), which is the deflection optical lever sensitivity (Def OLS). And the Inverse Def OLS is determined by taking the inverse of the slop of the plot ($\Delta z/\Delta v$) nm/volts. Next, the cantilever spring

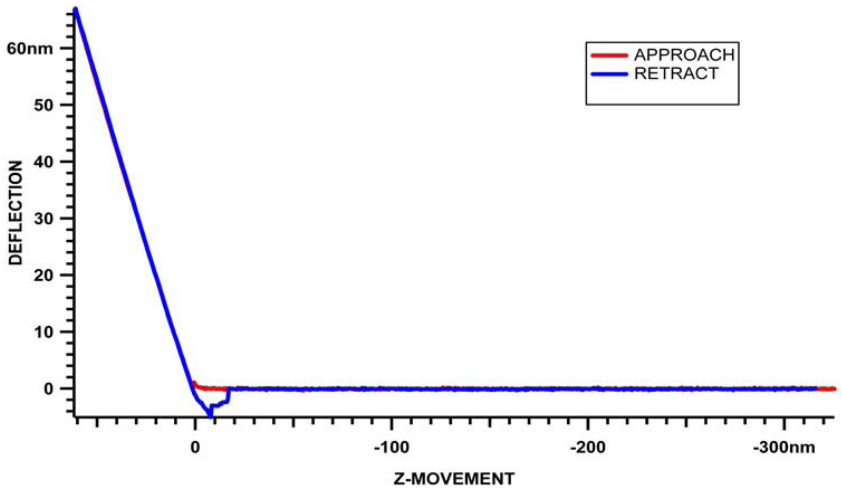

Figure 2.5 AFM force versus distance curve. Cantilever deflection versus Z-piezo movement. The force-distance curve was obtained on a bare region of the glass substrate to calibrate the optical lever sensitivity and shows the approach and retract curve.

constant (K) was determined, using the thermal noise method. The spring constant of the cantilever is the stiffness of the cantilever expressed in terms of Newtons/meter (N/m). Commercial cantilevers are provided with a nominal spring constant from the manufacturer, which can differ from batch to batch. As a consequence, the spring constant K of the cantilever needs to be accurately determined prior to taking any measurements. Once the spring constant of the cantilever has been determined, then it enables the deflection of the cantilever, in meters, to be converted to force (N). Determination of the cantilever spring constant can be achieved using a number of methods, most AFM are equipped to calibrate the cantilever using the thermal noise method (*32*), which is usually software driven. With this method the AFM cantilever is thermally excited, which causes the cantilever to oscillate. It then relates the measured thermal noise in the AFM cantilever deflection signal to the spring constant of the cantilever. From the Inverse Def OLS (nm/volts) and the cantilever spring constant (N/m), the loading force can be calculated by deflection of the cantilever (volts). After engaging the tip to the surface, the loading force was kept to 1.0 nN in order to minimize sample damage and displacement.

AFM Tapping mode imaging in fluid

Silicon-nitride cantilevers (spring constant 0.027 N/m, length 60 μm, Biolever, Olympus, Tokyo, Japan) were used for all tapping mode imaging. Tapping mode imaging was conducted using 60 μm-long Biolever cantilevers (Olympus, Tokyo, Japan), which had a resonance frequency of 37 kHz in air. Thermal stabilization and determining the cantilever spring constant (K) was the same as described above for contact mode. The amplitude optical lever sensitivity (Amp OLS) was determined from amplitude versus distance plots (amplitude (volts) versus z-movement (meters)) on a bare region of the glass substrate, with the scan size set at 0 μm. From the Inverse Amp OLS (nm/volts), the free oscillation amplitude of the cantilever can be calculated in

nanometers and adjusted by the drive amplitude. The drive amplitude is the amplitude of the drive signal that goes to the piezo in order to drive the cantilever for predetermined free oscillation amplitude of the cantilever. As the drive amplitude goes up, so should the cantilever amplitude. The free oscillation amplitude has to be reduced in order to image live cells with the lower force. The free-oscillation amplitude of the cantilever was set to 100 nm. The set point parameter was decreased by the smallest increment (10 ~ 30 % of free amplitude) allowing for minimal force on the sample, as shown in Figure 2.6. The drive frequency used for imaging in liquid was set at the nominal resonance frequency of 6 ~ 8 kHz. All AFM data were composed of 128 scan lines and 128 pixels per line and the scan speed was usually 3 μm/s. First order flattening was performed using MFP-3D image processor.

2.4.2 Performance of the CLSM

The surface structure of fluorescently labeled cells was investigated with our custom-built combined AFM-CLSM system (Figure 2.1). The combined microscopes perform the AFM and CLSM measurements sequentially. Firstly, the fluorescence images were collected with an appropriate objective lens by CLSM. In order to get a three-dimensional image, we collected the depth-resolved (z-stacked) fluorescence images of neurons. The fluorescent image was recorded at an acquisition time of 4 ms per pixel. Right after confocal imaging, the same sample was imaged with AFM in contact mode or tapping mode. The detailed parameter for confocal imaging is described in the measurement and analysis section of each chapter.

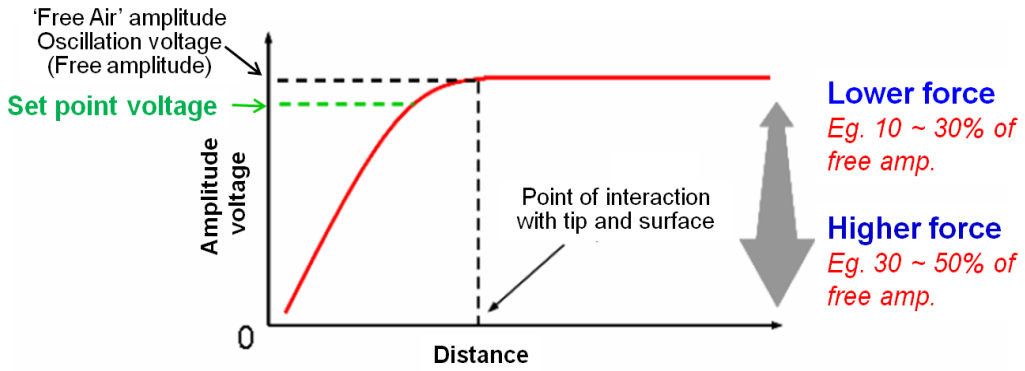

Figure 2.6 Conceptual amplitude voltage versus distance for Tapping mode imaging. Lower set point values result in higher tip-sample force; higher set point values result in lower tip-sample forces. This is not to scale and not real data.

2.5 Data Analysis

2.5.1 Data processing for the integration between AFM and CLSM images: Matlab routine

In order to localize the fluorescently labeled proteins to corresponding cellular structure, three-dimensional AFM image and three-dimensional CLSM image of the same region were integrated by our program using Matlab7.0.4 (The MathWorks Inc.). Because the scan range of CLSM image included that of AFM image, we cropped the CLSM image to match the position of the subject in both images. When both image sizes of AFM and CLSM were matched each other, a text file, which provided the height information of the structure, was created with the z- coordinates of every pixel from AFM data. And the other text files, which provided the fluorescent information of every voxel, were created with the value of fluorescent intensity of each pixel in every focal plane. They could be integrated by implementing our integration program using Matlab. Our Matlab routine is designed to three-dimensionally match and combine the one text file, originate from AFM and the other text file originated from CLSM. Thus, it can provide the cross-section views of the X-Z plane from the integrated AFM and CLSM image, which show fluorescent signal profiles on the cell's surface morphology. Appendix 1 provides a representative MATLAB script for Figure 2.9 (F-1).

2.6 Results

2.6.1 AFM imaging of neuronal cells under fixed and live conditions

Cultured neuronal cells can be seen by AFM under both fixed and live conditions.

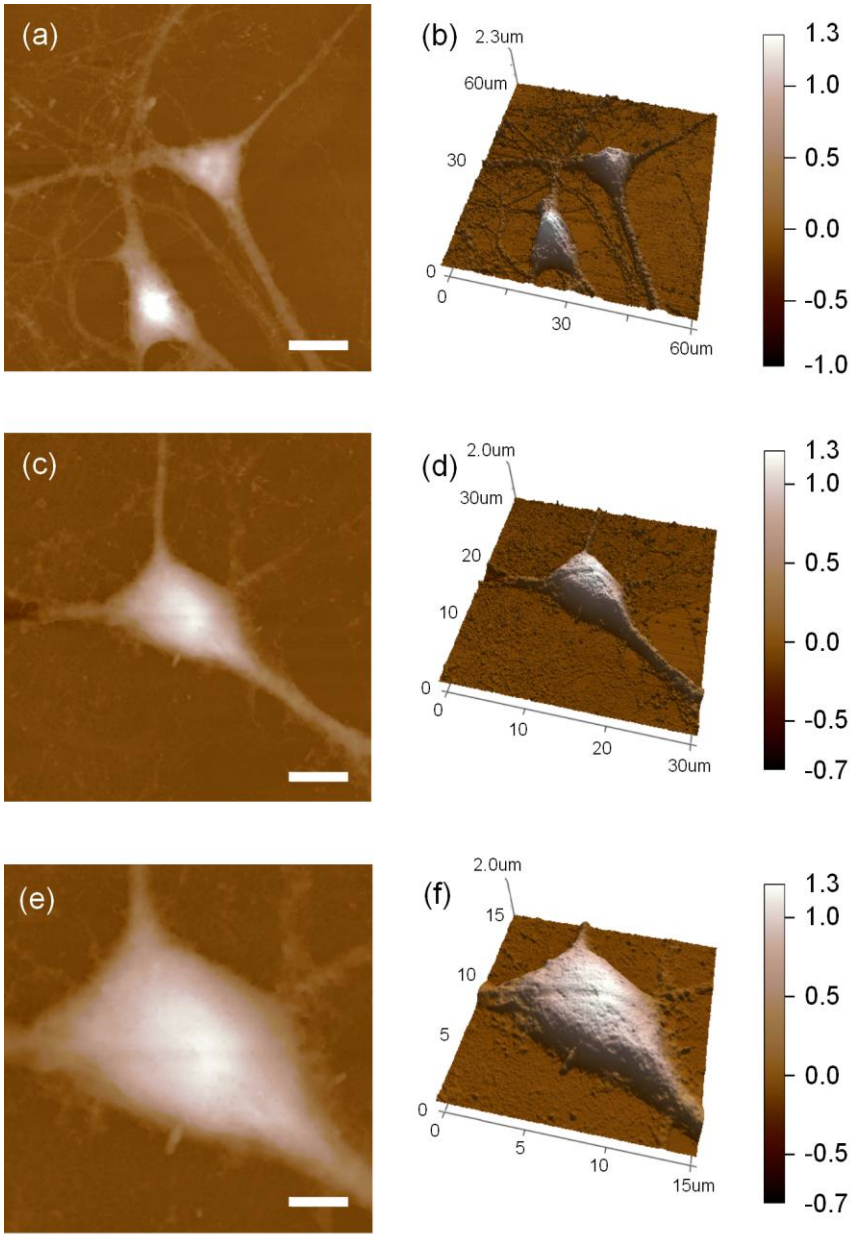

Figure 2.7 AFM Contact mode measurements of mouse hippocampal neurons. (a, c) Two-dimensional height images of hippocampal neurons, and (e) a magnified image of soma region shown in (c). Scale bars, (a) 20 μm, (b) 10 μm and (c) 5 μm. The long diameter of the neuron soma was 13.46 μm, and the height of it was 1.20 μm (Figure 2.7 (c)). (b, d and f) Three-dimensional surface reconstruction of hippocampal neurons shown in (a), (c), and (e), respectively. Scale bar represents values in μm.

Firstly, Figure 2.7 shows detailed topographic structures in cultured hippocampal neurons, which were prepared by fixation and dehydration by Contact mode AFM. The image shows the nm scale topography of the cell surface and the cell's maximal height and width of the neuron somata and neurites. The long diameter of the neuron soma was 13.46 μm, and the height of it was 1.20 μm (Figure 2.7 (c)). The width of the somata was ranging from 12.20 μm to 20.22 μm, and the height of them was ranging from 1.20 μm to 2.40 μm. The width of the neurites was ranging from 2.36 μm to 6.59 μm, and the height of them was ranging from 0.26 μm to 0.54 μm. These values were smaller than the average value reported in the previous study (*33*), in which the structures of mouse hippocampal neurons was also investigated with Contact AFM. Additionally, we can observe the detailed topography of the soma surface, which appears lumpy, in the magnified image (Figure 2.7 (e)). These AFM images on the same region could be obtained repeatedly (data not shown), indicating that our AFM imaging condition was optimized.

Secondly, Figure 2.8 shows detailed morphology of subcellular structures in live *Aplysia* sensory neurons by Tapping mode AFM. Intact morphologies and accurate dimensions of varicosity and multiple neurites of *Aplysia* sensory neurons without any treatment were obtained in a nanometer scale. The long axis diameter of the imaged varicosities was varied, ranging from 4.11 μm to 16.20 μm, and the height of them was ranging from 1.01 μm to 3.84 μm. The width of the neurites existing separately from other neurites was ranging from 1.66 μm to 4.96 μm, and the height of them was ranging from 0.35 μm to 0.84 μm. The dimensions of varicosities and neurites in intact *Aplysia* sensory neuron were firstly reported in this study. Although AFM is the most suitable tool for measuring accurate topography of the objects, there are several inherent weaknesses of applying AFM to live cell imaging. Due to the softness of the live cell membrane, mechanical forces from AFM tips attaching the cells for imaging generally press down the membrane and cause the measured heights slightly less than the actual

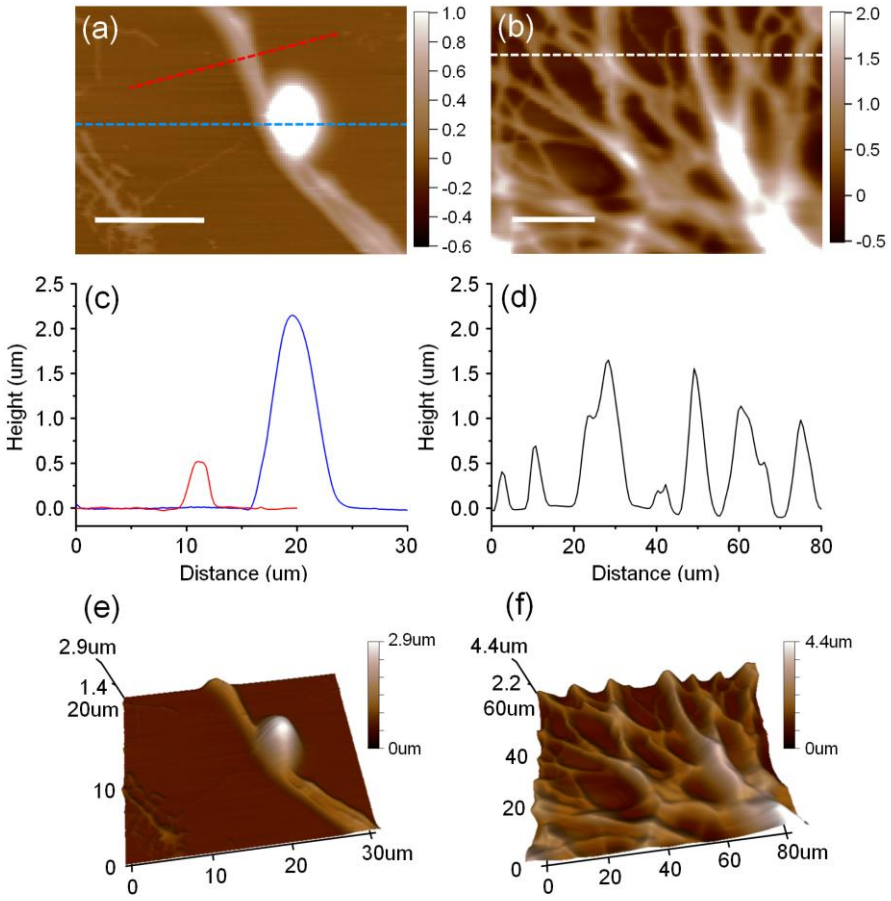

Figure 2.8 AFM Tapping mode measurements of *Aplysia* sensory neurons. Two-dimensional height images of (a) a varicosity located in the middle of neurite, and (b) multiple neurites. Scale bar represents values in μm. (c, d) The cross-section views along the dash line in (a) and (b), respectively. The varicosity in (a) exhibited a width of 7.78 μm and a height of 2.75 μm. The neurite in (b) exhibited a width of 2.75 μm and a height of 0.52 μm. (e, f) Three-dimensional surface reconstruction of a varicosity and neurites shown in (a) and (b), respectively. Scale bars, (a) 10 μm and (b) 20 μm.

values (*16*). Additionally, since AFM imaging is influenced by 'tip artifact', which is caused by convolution between the shape of the probe and the shape of the sample, their true widths are slightly narrower than those measured by AFM (*34*). However, when live *Aplysia* neurons were imaged with AFM by applying the minimal force, the surface of the varicosity and neurites appear comparatively smooth without any bumps on it, indicating that our AFM imaging technique was highly adaptable for imaging intact structures of cultured *Aplysia* neurons.

2.6.2 Integrated images acquired by the combined AFM and CLSM system

We next compared and integrated AFM images with CLSM images taken in the same varicosities and neurites of *Aplysia* sensory neurons cocultured with motor neurons (Fig. 2.9). The cytoplasm of sensory neuron was visualized by mRFP expression (Fig. 2.9(a)). In the sensory neuron, the synaptic vesicles tagged with synaptophysin-eGFP were observed within the cytoplasm (Fig. 2.9(b)). In contrast to confocal images, overall topography of both sensory and motor neuron among coculture was shown in AFM height image (Fig. 2.9(c)). Prior to three-dimensional image integration, 2D CLSM image originated from one focal plane was overlaid on AFM 2D height image to estimate the difference between the shape of cells in AFM image and those in CLSM image (Fig. 2.9(d) and (e)). The region overlapped with mRFP fluorescent signal was sensory neuron and the other region was motor neuron. However, as shown in Fig. 2.9(d), the neurites of sensory neuron (two white arrows) were not clearly observed from red fluorescent image. Although the mRFP protein is expressed evenly throughout the cytoplasm and this signal must show a general topography of sensory neurons by optical imaging, it was evident that the fine structure such as

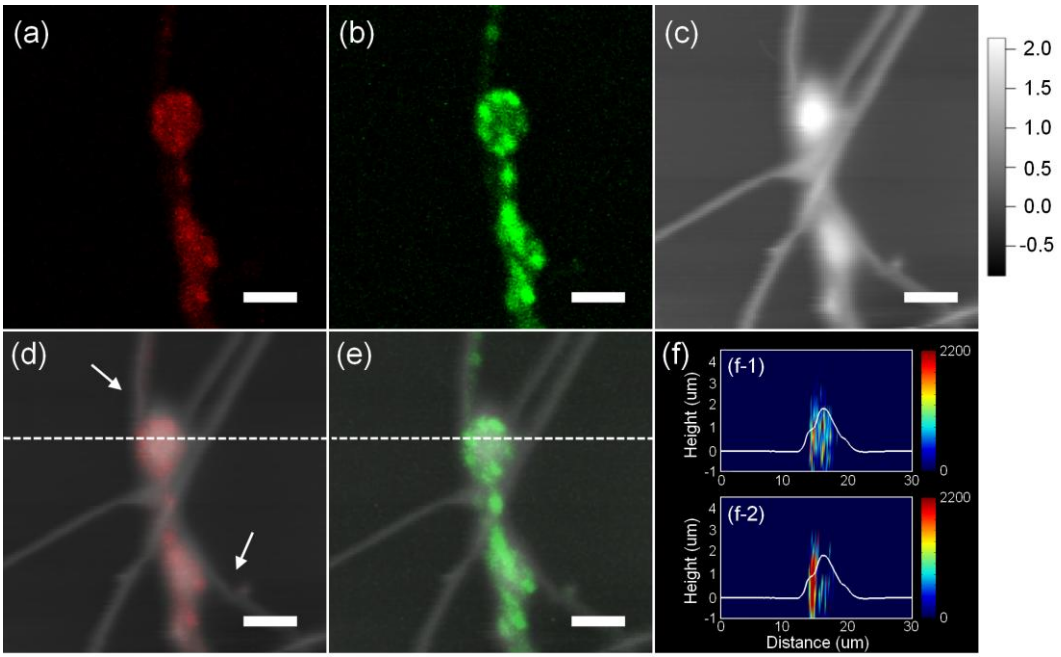

Figure 2.9 Comparison of AFM and CLSM data obtained from study of the varicosities on sensory neuron among *Aplysia* coculture. Both synaptophysin-eGFP and mRFP were expressed in the sensory neuron, which is cocultured with the motor neuron prior to imaging. (a, b) Two-dimensional (2D) fluorescent CLSM image. The sensory neuron was labeled with both mRFP (a) and synpatophysin-eGFP (b). (c) 2D height image of AFM AC mode image. Gray scale bar represents values in μm. (d, e) 2D height image overlaid with 2D fluorescent image of mRFP (d) and synaptophysin-eGFP (e). (f) Cross-section views of the merged AFM and CLSM (3D) images marked in (d) and (e) (a view of xz plane) are shown in (f-1) and (f-2), respectively. White line shows cell surface, and color scale spectrum shows fluorescent intensity. Scale bars, 5 μm.

neurites labeled with mRFP signal showed discrepancy with actual overall shape measured by AFM due to insufficient extent of expressed proteins for detection. Therefore, AFM height image is adequate for investigation of actual structure. Next, we applied our newly developed Matlab routine to integrate three-dimensional AFM surface plot of height image (in nanometer scale resolution) with three-dimensional CLSM fluorescent images taken by serial Z-sectioning (in laterally 330 nm, axially 1.9 um resolution). The cross-section views of integrated AFM and CLSM image marked on Fig. 2.9(d) and 2.9(e) were shown in Fig. 2.9(f). The cytoplasmic regions within the varicosity and the localization of synaptic vesicles within the varicosity can be shown in relation to the 3D morphology of neuron. Because CLSM lateral resolution is higher than axial resolution, 3D fluorescent signals are observed vertically oval. It was shown three-dimensionally that cytoplasmic regions were evenly distributed over the varicosity, and synaptic vesicles were localized on the left part of varicosity. When 3D CLSM image complementarily combines with AFM 3D image, the accurate dimension of cellular structure can be acquired by AFM part and 3D intracellular mapping of functional components can be acquired by CLSM part. Therefore, our integration method between 3D AFM and 3D CLSM images are more suitable than simple 2D confocal images to study the relation between structure and function in the live or fixed neuron cells.

2.7 Conclusions

The combined AFM and CLSM system provides detailed structural information about the neuronal cells under fixed and live conditions by AFM part, and the intracellular mapping of fluorescent signal within the cells by CLSM part. With the developed integration program, 3D topography of neuronal cells could be integrated with 3D fluorescent signals of the same cells. From the integrated images, we can

analyze more accurate correlation between structure and function. Additionally, this combined study can be performed in the course of time. Thus, this system is efficiently applied to measure accurate and detailed morphological changes or volumetric changes together with functional changes in neuronal structure.

2.8 References

(1) Hirokawa, N., Sobue, K., Kanda, K., Harada, A., and Yorifuji, H. (1989) The Cytoskeletal Architecture of the Presynaptic Terminal and Molecular-Structure of Synapsin-1. *J Muscle Res Cell M 10*, 270-270.

(2) Nimchinsky, E. A., Sabatini, B. L., and Svoboda, K. (2002) Structure and function of dendritic spines. *Annual Review of Physiology 64*, 313-353.

(3) Sankaranarayanan, S., Atluri, P. P., and Ryan, T. A. (2003) Actin has a molecular scaffolding, not propulsive, role in presynaptic function. *Nat Neurosci 6*, 127-135.

(4) Prince, J. S., Lynn, M. J., and Blackwelder, P. L. (2006) White vesicles in the skin of Aplysia californica cooper: A proposed excretory function. *J Mollus Stud 72*, 405-412.

(5) Nikonenko, I., Jourdain, P., and Muller, D. (2003) Presynaptic remodeling contributes to activity-dependent synaptogenesis. *Journal of Neuroscience 23*, 8498-8505.

(6) Hu, X. D., Viesselmann, C., Nam, S., Merriam, E., and Dent, E. W. (2008) Activity-Dependent Dynamic Microtubule Invasion of Dendritic Spines. *Journal of Neuroscience 28*, 13094-13105.

(7) Gomes, R. A., Hampton, C., El-Sabeawy, F., Sabo, S. L., and McAllister, A. K. (2006) The dynamic distribution of TrkB receptors before, during, and after synapse formation between cortical neurons. *Journal of Neuroscience 26*, 11487-11500.

(8) Triller, A., Rostaing, P., Korn, H., and Legendre, P. (1997) Morphofunctional evidence for mature synaptic contacts on the Mauthner cell of 52-hour-old zebrafish larvae. *Neuroscience 80*, 133-145.

(9) Bailey, C. H., Thompson, E. B., Castellucci, V. F., and Kandel, E. R. (1979) Ultrastructure of the synapses of sensory neurons that mediate the gill-withdrawal reflex in Aplysia. *J Neurocytol 8*, 415-44.

(10) Yamada, K., Fukaya, M., Shibata, T., Kurihara, H., Tanaka, K., Inoue, Y., and Watanabe, M. (2000) Dynamic transformation of Bergmann glial fibers proceeds in correlation with dendritic outgrowth and synapse formation of cerebellar Purkinje cells. *Journal of Comparative Neurology 418*, 106-120.

(11) Binnig, G., Quate, C. F., and Gerber, C. (1986) Atomic force microscope. *Phys Rev Lett 56*, 930-933.

(12) Hoh, J. H., and Hansma, P. K. (1992) Atomic force microscopy for high-resolution imaging in cell biology. *Trends Cell Biol 2*, 208-13.

(13) Ohnesorge, F. M., Horber, J. K., Haberle, W., Czerny, C. P., Smith, D. P., and Binnig, G. (1997) AFM review study on pox viruses and living cells. *Biophys J 73*, 2183-94.

(14) Muller, D. J., Hand, G. M., Engel, A., and Sosinsky, G. E. (2002) Conformational changes in surface structures of isolated connexin 26 gap junctions. *EMBO J 21*, 3598-607.

(15) Barrera, N. P., Herbert, P., Henderson, R. M., Martin, I. L., and Edwardson, J. M. (2005) Atomic force microscopy reveals the stoichiometry and subunit arrangement of 5-HT3 receptors. *Proc Natl Acad Sci U S A 102*, 12595-600.

(16) Xiong, Y., Lee, A. C., Suter, D. M., and Lee, G. U. (2009) Topography and nanomechanics of live neuronal growth cones analyzed by atomic force microscopy. *Biophys J 96*, 5060-72.

(17) Jena, B. P. (2006) Cell secretion machinery: studies using the AFM. *Ultramicroscopy 106*, 663-9.

(18) McNally, H. A., and Borgens, R. B. (2004) Three-dimensional imaging of living

and dying neurons with atomic force microscopy. *J Neurocytol 33*, 251-8.

(19) Schneider, S. W., Pagel, P., Rotsch, C., Danker, T., Oberleithner, H., Radmacher, M., and Schwab, A. (2000) Volume dynamics in migrating epithelial cells measured with atomic force microscopy. *Pflugers Arch 439*, 297-303.

(20) Pawley, J. B. (1995) *Handbook of biological confocal microscopy*, 2nd ed., Plenum Press, New York.

(21) Madl, J., Rhode, S., Stangl, H., Stockinger, H., Hinterdorfer, P., Schutz, G. J., and Kada, G. (2006) A combined optical and atomic force microscope for live cell investigations. *Ultramicroscopy 106*, 645-51.

(22) Lieberman, K., BenAmi, N., and Lewis, A. (1996) Fully integrated near-field optical, far-field optical, and normal-force scanned probe microscope. *Rev Sci Instrum 67*, 3567-3572.

(23) Noy, A., and Huser, T. R. (2003) Combined force and photonic probe microscope with single, molecule sensitivity. *Rev Sci Instrum 74*, 1217-1221.

(24) Kellermayer, M. S. Z., Karsai, A., Kengyel, A., Nagy, A., Bianco, P., Huber, T., Kulcsar, A., Niedetzky, C., Proksch, R., and Grama, L. (2006) Spatially and temporally synchronized atomic force and total internal reflection fluorescence microscopy for imaging and manipulating cells and biomolecules. *Biophysical Journal 91*, 2665-2677.

(25) Kondra, S., Laishram, J., Ban, J., Migliorini, E., Di Foggia, V., Lazzarino, M., Torre, V., and Ruaro, M. E. (2009) Integration of confocal and atomic force microscopy images. *J Neurosci Methods 177*, 94-107.

(26) Gradinaru, C. C., Martinsson, P., Aartsma, T. J., and Schmidt, T. (2004) Simultaneous atomic-force and two-photon fluorescence imaging of biological specimens in vivo. *Ultramicroscopy 99*, 235-45.

(27) Park, J. W., Park, A. Y., Lee, S., Yu, N. K., Lee, S. H., and Kaang, B. K. (2010) Detection of TrkB receptors distributed in cultured hippocampal neurons through bioconjugation between highly luminescent (quantum dot-neutravidin) and (biotinylated anti-TrkB antibody) on neurons by combined atomic force

microscope and confocal laser scanning microscope. *Bioconjug Chem 21*, 597-603.

(28) Kassies, R., van der Werf, K. O., Lenferink, A., Hunter, C. N., Olsen, J. D., Subramaniam, V., and Otto, C. (2005) Combined AFM and confocal fluorescence microscope for applications in bio-nanotechnology. *J Microsc 217*, 109-16.

(29) Vie, V., Giocondi, M. C., Lesniewska, E., Finot, E., Goudonnet, J. P., and Le Grimellec, C. (2000) Tapping-mode atomic force microscopy on intact cells: optimal adjustment of tapping conditions by using the deflection signal. *Ultramicroscopy 82*, 279-88.

(30) Le Grimellec, C., Lesniewska, E., Giocondi, M. C., Finot, E., Vie, V., and Goudonnet, J. P. (1998) Imaging of the surface of living cells by low-force contact-mode atomic force microscopy. *Biophys J 75*, 695-703.

(31) Braet, F., DeZanger, R., Kammer, S., and Wisse, E. (1997) Noncontact versus contact imaging: An atomic force microscopic study on hepatic endothelial cells in vitro. *Int J Imag Syst Tech 8*, 162-167.

(32) Hutter, J. L., and Bechhoefer, J. (1993) Calibration of Atomic-Force Microscope Tips (Vol 64, Pg 1868, 1993). *Rev Sci Instrum 64*, 3342-3342.

(33) Yingge, Z., Xia, J., and Lan, S. (2003) The relations between neurite development and the subcellular structures of hippocampal neuron somata. *J Struct Biol 144*, 327-36.

(34) Eaton, P., and West, P. (2010) *Atomic force microscopy*, Oxford University Press Inc, New York.

Chapter III.

Detection of TrkB receptors distributed in cultured Hippocampal neurons

3.1 Introduction

Currently, researches in neuroscience have been focused on the fundamental understanding of ligand (or neurotrophins)-receptor interaction mechanism, the localization of receptors on the surface of neurons, and receptor-bound signal trafficking. Neurotrophins are a family of growth factors regulating differentiation, maturity, and survival of neurons. The diverse functions of neurotrophins are mediated by their specific interaction with tyrosine kinase receptors (*1*). The tyrosine kinase receptors (Trks) include TrkA (a receptor for nerve growth factor (NGF)), TrkB (a receptor for brain-derived neurotrophic factor (BDNF) and neurotrophin-4/5 (NT-4/5)), and TrkC (a receptor for neurotrophin-3 (NT3)). Lohof et al. was the first to show neurotrophin-evoked increases in synaptic transmission (*2*). Specially, BDNF has emerged a major regulator of synaptic transmission and plasticity at adult synapses in many regions of the CNS (central nervous system). Due to this unique role of BDNF, of all the neurotrophins, BDNF/TrkB (Tyrosine Kinase B) is the only signaling system exhibiting widespread distribution across the subregions of the hippocampus and the adult forebrain (*3*). The binding of BDNF to TrkB receptor activates down-stream intracellular cascades, regulating neuronal development and plasticity, long-term potentiation (LTP), long-term depression (LTD), which is certain forms of short-term synaptic plasticity, and apoptosis (*4-5*). BDNF treatment of embryonic or early postnatal hippocampal neurons results in a transient potentiation excitatory synaptic transmission lasting 10 – 20 min following washout (*6*). In contrast, application of BDNF for several minutes can trigger a long-lasting increase in synaptic efficiency dubbed BDNF-induced LTP (*4, 7*). Additionally, genetic ablation of TrkB gene in the forebrain changes hippocampal spine density and length in an age- and region-specific manner, which in turn may affect synaptic transmission and plasticity. The hippocampus is best

recognized for its role in declarative memory and spatial learning (*8*). To understand the pathogenic mechanism related to the BDNF/TrkB signaling as well as the development and regulation of the nervous system, it is important to monitor the localization of TrkB receptors on hippocampal neurons.

For several decades, an immunocytochemical method has been developed to detect antigens (e.g. extracellular surface of membrane receptors) using antigen-antibody reaction. To visualize antigens with an optical microscope or electron microscope, antibodies combined to antigens have to be labeled with various multiple fluorescent dyes or by the avidin-biotin peroxidase complex, respectively (*9-10*). And, the intracellular distribution of TrkB receptor protein, and the relation between TrkB and BDNF pattern were studied mostly (*11-13*). Thus, the distribution of TrkB receptor on the cell surface, which had been targeting to the surface membrane for receptor function, has to be determined to understand the BDNF/TrkB signaling or BDNF-induced LTP. Additionally, the studies on the localization of endogenous receptor patterns related to three-dimensional topography of neuronal cells will help to elucidate cellular mechanism related to TrkB receptors.

In order to investigate the localization of TrkB receptors, we labeled them with highly luminescent, no-photobleaching and photostable fluorescent QDs. Semiconductor quantum dots with broad absorption, high extinction coefficient, high luminance, narrow and tunable emission wavelength through the adjustment of their size are ideal fluorophores as biological tagging materials (*14-16*). In addition, compared with conventional organic dyes or fluorescent proteins, QDs have high photostability and can resist to photobleaching for a prolonged time of AFM-CLSM measurement (*17-19*). QDs have been used for protein and DNA immunoassays, fluorescence resonance energy transfer (FRET), diagnostics, live cell imaging through bioconjugation, and high-throughput screening. At present, bioconjugates of QDs bound to ligands such as streptavidins, neutravidins, and biotinylated proteins, are excellent

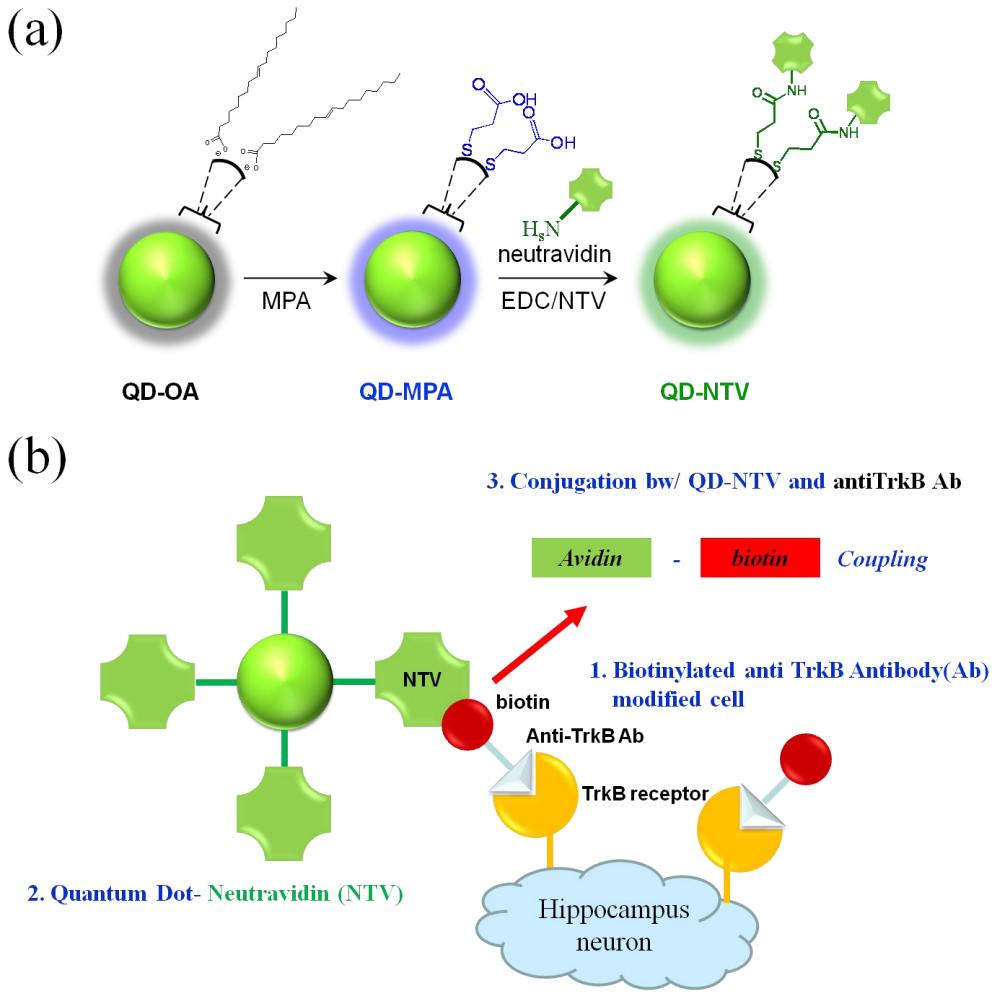

Scheme. 3.1. Synthesis of QD-NTV conjugates. (a) Schematic illustration of the preparation of QD-NTV conjugates. From left to right: QD-OA, QD-MPA, and QD-NTV (neutravidin) conjugates (b) Schematic representation depicting of detection of TrkB receptors on a mouse hippocampus nerve cell through (QD-NTV)-(biotinylated anti TrkB antibody) conjugation

tools for the study of neuroscience. In this study, we synthesize the highly luminescent water-soluble QD-neutravidin (NTV) bioconjugates and detect the TrkB receptors, on cultured hippocampal neurons with QD-NTV bioconjugates. QD-NTV bioconjugates interact with TrkB receptors, pretreated with biotinylated anti-TrkB receptor antibody and located in cultured hippocampal neurons, via a high affinity between avidin and biotin, as indicated in Scheme 3.1. The distribution of TrkB receptors in cultured hippocampal neurons was observed three-dimensionally by AFM-CLSM at nanometer-scale spatial resolution combined with optical fluorescence images.

3.2 Experimental Section

3.2.1 Chemicals

Cadmium oxide (CdO, 99.99%), zinc acetate (99.9% powder), selenium (99.9%, powder), sulfur (99.9%, powder), trioctylphosphine (TOP, 90%) , oleic acid (OA, 90%), 1-octadecene (ODE, 90%), mercaptopropionic acid (MPA, 99.8%), 1-ethyl-3-(3-dimethylaminopropyl)carbodiimide (EDC), N-hydroxysuccinamide (NHS), sephadex G-25 (beads for gel-filtration), Agarose for gel electrophoresis, sodium phosphate dibasic heptahydrate (for PBS buffer solutions, ACS reagent grade), sodium dihydrogen phosphate dehydrate (for PBS buffer solutions), Trizma base (minimum 99.9% titration) and acetic acid (glacial) for Tris-Acetate EDTA (TAE) buffer solutions, brilliant blue R and bromophenol blue sodium salt for electrophoresis and biological analysis, ethylene diamine tetra acetic acid sodium salt (EDTA sodium salt), paraformaldehyde were purchased from Sigma Aldrich. Neutravidin (NTV) was purchased from Pierce. Biotinylated antibody against mouse TrkB extracellular domain (BAF1494), which is polyclonal full length goat IgG, was purchased from R&D system. Hexane, methanol,

ethanol, acetone, and chloroform were purchased from Daejung chemicals. All chemicals were used as purchased without further purification. Buffer solutions are home-made.

3.2.2 Single-step synthesis of quantum dots with chemical composition gradients

The highly luminescent green-emitting (the emission wavelength is 520 nm with a FWHM of less than 30 nm) CdSe/ZnS quantum dots with chemical composition gradients were produced by our previously-reported single-step synthetic method (*20*). 0.10 mmol of CdO, 4 mmol of zinc acetate, and 12.6 mmol of oleic acid were placed in a 100 ml two-neck round-bottom flask. The mixture was heated to 200 ℃, degassed under 100 mtorr pressures for 30 min, filled with N_2 gas. The mixture of $Cd(OA)_2$ and $Zn(OA)_2$ was allowed to cool to room temperature and kept in the glove box. 1.2 mmol of Se powder and 12 mmol of S powder dissolved in 10 ml of TOP were dissolved into 100 ml two-neck flask and heated to 200 ℃ under N_2 condition. After Se-S was completely dissolved, the mixture yellow change into transparent. The mixture was allowed to cool to room temperature and kept in the glove box. The synthesis of CdSe/ZnS quantum dot was wet chemical synthesis. $Cd(OA)_2$ and $Zn(OA)_2$ solution and 16 ml of 1-octadecene were loaded in a 100 ml three-neck round-bottom flask (degassed under 100 mTorr pressure for 20 ~ 30 min, filled with N_2 gas) and further heated to 310 ℃ to form a clear solution of $Cd(OA)_2$ and $Zn(OA)_2$. At this temperature (305 ℃; nucleation temperature), 2.8 ml of Se-S precursor was quickly injected into the reaction flask. After the injection, the temperature of the reaction flask was set to 300℃ for promoting the growth of QDs. We grew QDs at this temperature for 10 min, and removed heating mantle. It was then cooled down to room temperature to stop the

growth. In order to remove excess surfactant (TOP, OA), all reaction products were dissolved in 5 ml chloroform, 20 ml excess methanol was subsequently added to the CdSe/Zns QD solution. Centrifugation and decantation were performed to remove excess surfactants. All these procedures were repeated 3 times.

3.2.3 Surface modification of CdSe/ZnS QDs

Water-soluble QDs were prepared by replacing the oleic acid (OA, originally coordinated ligand) attached to the surface of QDs with mercaptopropionic acid (MPA) as follows (*20-21*). 10 mg of QDs dispersed in 10 ml of chloroform was placed in a two-neck round-bottom flask, and heated to 70 ~ 80 ℃. 2 ml of MPA was dropped to the solution. MPA capped QDs solution changed into turbid. The reaction was held in 1 hr with mild stirring, and cooled down to room temperature. The MPA-capped QDs were extracted by centrifugation, purified twice with chloroform, and finally dissolved into PBS buffer of pH 7.4. In PBS buffer, turbid MPA-capped QDs solution changed into clear solution, because of the pKa value of MPA (4.87). We kept MPA-capped QDs in PBS buffer at 4 ℃ in refrigerator.

3.2.4 Conjugation between MPA-capped QDs and neutravidin (NTV)

The conjugation was carried out through a coupling reaction between the carboxyl group of MPA and the amino group of NTV using EDC as the coupling activator (*22*). The concentration ratio of QD-MPA to NTV is 1:40 in mole. The conjugation of QD-MPA dispersed in PBS buffer with NTV was done as it followed. The 100 μl of 2 mM EDC dissolved in 0.2 M of 2-(morpholino) ethanesulfonic acid (MES) of pH 6.0 was added to the QD solution, and then the resulting solution was stirred mildly for 5 min.

The 50 μl of 5 mM NHS dissolved in 0.2 M of MES of pH 6.0 was added to the e-tube mixture under mild stirring for 30 min at room temperature. The mixture was purified by size exclusion chromatography using sephadex G-25. Only QDs reacted with EDC and NHS were collected. Then, 5 μl of NTV taken from the stock solution (stock solution: 10mg dissolved in 1ml of 0.2 M borate buffer of pH 9.5) was diluted with 95 μl of 0.2 M borate buffer of pH 9.5, and then this solution was added to the solution containing QDs reacted with EDC and NHS. The solution was stirred at room temperature for 2 h, and QD-NTV was purified by Sephacryl S-400 HR size exclusion spin column (GE healthcare, Sweden).

3.2.5 Cell culture

Primary hippocampal neurons were cultured from mice embryo E18 (ICR strain) by modified protocol from Banker *et al.* (*23*). Briefly, pregnant ICR mice were euthanized to decapitate fetus and dissect out the fetal brains. Hippocampi were removed under a dissecting microscope and trypsinized with 2.5 % trypsin solution in distilled water. Then, neurons were dissociated and plated on the poly-L-lysine-coated glass bottom culture dishes in a concentration of 50000/cm^2. Neurons were grown for two weeks in maintenance medium (neurobasal medium containing 2 % B-27, 1mM glutamine, and penicillin/streptomycin) before fixation.

3.2.6 Cell fixation

For the detection of TrkB receptors, mouse hippocampal neurons were fixed with 4% paraformaldehyde on ice for 10 min. Then, we washed the cells with PBS more than 3 times. In order to reduce the non-specific binding, the cells were blocked with 2 %

(wt/volume) of BSA dissolved in PBS for overnight at 4 ℃. Next day, we washed the cells with PBS more than 3 times.

3.2.7 Detection of TrkB receptors on a mouse hippocampus neuron cell surface

Biotinylated anti-TrkB antibodies and QD-NTV were diluted in PBS. Fixed and BSA-blocked primary neurons were incubated with 5 μg/ml of a mouse anti-TrkB antibody that recognized the extracellular domain of a TrkB receptor (catalog no. BAF 1494; R&D systems) for 2 hr at room temperature. Then, the neurons were washed with PBS several times to eliminate the non-specific binding of biotinylatated anti-TrkB antibody. Next, we sequentially incubated the neurons with 160 nM of QD-NTV for 2 hr at room temperature. During this incubation, final bioconjugation of biotinylated anti-TrkB antibody with QD-NTV via avidin-biotin coupling was made at the cell surface where TrkB receptors were located. For an optical microscope measurement, neuron cells were examined right after a QD-labeling step. For combined atomic force and confocal microscopy measurements, neuron cells were dehydrated with 75, 90, and 100 % of ethanol in series and then they were air-dried.

3.3 Measurements and Analysis

3.3.1 Measurement of Quantum Yield (Q. Y.) of CdSe/ZnS QDs

The photoluminescence quantum yield (PL. Q.Y) of CdSe/ZnS QDs with chemical composition gradients dispersed in 0.2 M PBS buffer of pH 7.4 was measured and estimated by comparing their photoluminescence intensities with those of primary

standard dye solutions (emission close to the QDs, Coumarin 545 with the Q.Y of 0.95 in ethanol) at the same optical density (0.05) at the same excitation wavelength of 465nm. The room temperature PL. Q.Y. of the green-emitting QDs is typically ~ 80 %.

3.3.2 Transmission Electron Microscopy (TEM)

The TEM images of the QDs were obtained using a JEM-3010 (JEOL) to analyze their average size of QDs. Low-coverage samples were prepared by placing a drop of a dilute hexane dispersion of QDs on a copper grid (300 mesh) coated with an amorphous carbon film.

3.3.3 Fourier Transform Infrared Spectroscopy (FT-IR)

To confirm an amide bonding of QDs with NTV, we carried out the analysis of FT-IR vibration spectra of samples of QD-NTV (JASCO FT/IR-660 plus, made by JASCO).

3.3.4 Measurement of Hydrodynamic size of CdSe/ZnS QDs

Dynamic light scattering (DLS) analysis was performed at 25℃ using a DynaPro Dynamic Light Scatterer (Wyatt Technology, Santa Barbara, CA). Dynamic All QD samples were between 0.1 and 0.25 μM in the borate solution (0.01M, pH 8.0) and centrifuged down at 13200 rpm. The surpernants were filtered through 0.2 μm syringe filters before analysis. Laser wavelength used was 828.5 nm. Each autocorrelation function (ACF) was acquired for 10 sec, and averaged for 10 times per measurement. The resulting ACF was fitted using the Dynamics V6 software. Hydrodynamic radii were obtained from a mass-weighted size distribution analysis and reported as the mean

of triplicate measurements. The cuvette used was washed with 1% Triton × 100 (filtered).

3.3.5 Confocal Laser Scanning Microscopy (CLSM)

The confocal fluorescent images and differential interference contrast (DIC) images of QD-labeled hippocampus neurons were obtained using Fluoview FV1000 confocal laser scanning microscope (CLSM; Olympus, Tokyo, Japan) connected to an IX 81 inverted microscope (Olympus, Tokyo, Japan) with a UPLAPO 60X waterproof objective. QDs were excited with a 488 nm Ar^+ ion laser line and detected in the wavelength range of 510 ~ 530 nm. The confocal fluorescence images were overlaid with DIC images in order to locate the components of neuron cells in more informative way.

3.3.6 Combined AFM and CLSM

Fluorescent and nanometer-scale spatially-resolved structural images of QD-labeled cells were obtained with our custom-built combined AFM-CLSM system. In order to get a three-dimensional fluorescence image of neurons by CLSM, we collected the depth-resolved (i.e., z stack) fluorescence images of neurons in every 0.3 μm to obtain the magnified images. The whole image of neurons was reconstructed from all the z-stack fluorescence images. Neurons were imaged at a scan rate of 1.0Hz in the contact mode with an AFM. A 200 μm-long PNP-TR cantilevers (NanoWorld, Switzerland) with a spring constant of 0.08 N/m and a resonant frequency of 17 kHz was used. A tip radius of curvature is smaller than 10nm. The force of 1.0 nN was maintained during imaging. Integration between CLSM and AFM images was

performed in two ways. The first way is to overlay the 2D CLSM image, which was projected on x-y plane, on the AFM surface plots of height image. Since we used biotinylated anti-TrikB antibody against TrkB extracellular domain and did cytochemical assay without permeabilization to detect the localization of TrkB receptor on the cell surface, QD-NTV signal marked the position of TrkB receptor located on the cell surface (Figure 3.5). The second way is to combine 3D AFM surface topography with 3D CLSM image of the same region with help from the integration program using Matlab. (Figure 3.6)

3.4 Results and Discussion

We produced highly luminescent semiconductor quantum dots by our single-step synthesis of QDs with chemical composition gradients (*20*). In the bioconjugation study, we synthesized green CdSe/ZnS core/shell QDs with chemical composition gradients, which emit at 520 nm with a FWHM less than 30 nm (Fig. 3.1(a)). The average size of the CdSe/ZnS core/shell QDs is 9 nm in diameter with narrow size distribution, as shown in Figure 3.1 (a, inset). The unique structure of our QDs (QDs with gradual chemical composition gradient outward) has good merits: the relaxation of the strain caused by the lattice mismatch between the CdSe core and the ZnS shell even though the thickness of the outer part of the QDs is more than two atomic layers, funneling the excitons toward the cores of QDs due to chemical composition gradients (i.e. energy-gradient structure) and thus enhancing the photoluminescence. In order to use QDs for biological applications, we need to have water-soluble QDs. The QDs as produced by our single-step synthetic method were originally surface-passivated with oleic acid that functioned as a solvent and coordinating ligand. Water-soluble QDs were prepared by replacing the oleic acid (OA) coordinated to their surfaces with mercaptopropionic acid

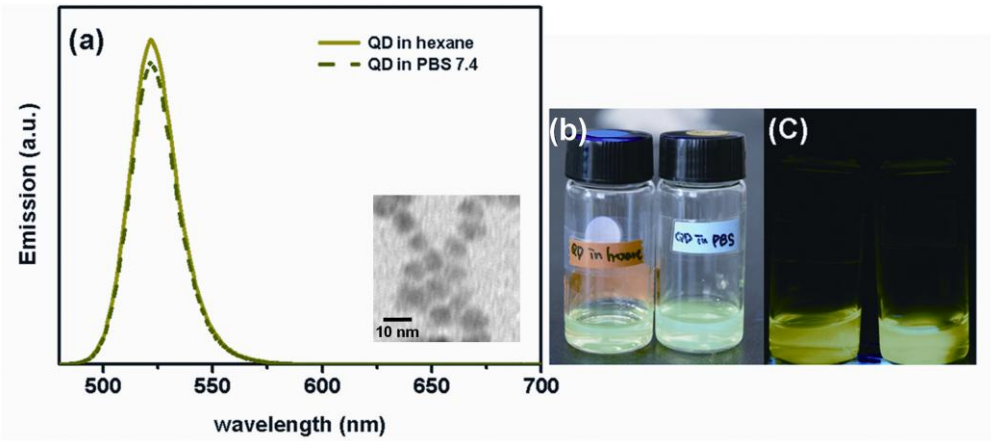

Figure 3.1 Optical characteristics of QDs and conjugated QDs. (a) Photoluminescence spectra of green-emitting CdSe/ZnS core/shell QDs with chemical composition gradient capped with oleic acids and dispersed in hexane (denoted with solid line) and those capped with MPAs and dispersed in PBS (denoted with dotted line). The average size of QD-OA is 9 nm in diameter (inset). (b) It shows high luminance of both QD-OAs dispersed in hexane and QD-MPAs dispersed in PBS under an indoor common fluorescent lamp. (c) It shows the photo of the same QDs irradiated with a UV lamp under the fluorescent lamp off.

(MPA) via a conventional ligand exchange reaction (*20-21*). The MPA-capped QD precipitates are collected out from the turbid mixture by several centrifugal purifications. We disperse MPA-capped QD (QD-MPA) in PBS buffer (pH 7.4). Figure 3.1(a) shows the photoluminescence spectra of green-emitting CdSe/ZnS core/shell QDs with chemical composition gradient (high quantum yield ~ 80 %) capped with oleic acids (OA), which was dispersed in hexane (denoted with solid line) and those capped with MPAs, which was dispersed in PBS (denoted with dotted line). As shown in Figure 3.1(a), water-soluble QD-MPA still maintains high quantum efficiency due to efficient substitution with MPA. Additionally, Figure 3.1(b) shows high luminance of both OA capped QD (QD-OA) dispersed in hexane and QD-MPA dispersed in PBS under an indoor common fluorescent lamp. Figure 3.1(c) shows the photoimages of the same QD-OA and QD-MPA irradiated with a UV lamp under the indoor common fluorescent lamp off. Our green-emitting CdSe/ZnS core/shell QDs with chemical composition gradients either capped with oleic acids (OA) or capped with MPAs are highly luminescent (measured to be ~ 80 % Q.Y., using a reference dye of coumarin 545 with 95 % of Q.Y in ethanol). Water-soluble QD-MPAs dispersed in PBS has been stable for more than a year at 4℃. Eventually in order to detect TrkB receptors on the neuron cells through the interaction between QD-neutravidin (QD-NTV) and biotinylated anti-TrkB antibody, we need to generate QD-NTV. A solution of NTV powder dissolved in 0.2 M borate of pH 9.5 is mixed with QD-MPA dispersed in PBS. The concentration of QD-MPA turns out 0.42μM and 10mg of NTV is dissolved in 1 ml of 0.2 M borate of pH 9.5, and thus that of NTV turns out to be 167 μM. The conjugation is made through a coupling reaction between the carboxyl group of MPA and an amino group of NTV using EDC as the coupling activator (*22*). After the coupling reaction, the mixture of QD-MPA, NTV, and QD-NTV was purified through gel filtration. QD-NTV conjugates are confirmed by the three following methods. In one way, samples were analyzed by electrophoresis on a 1% agarose gel in Tris acetate EDTA (TAE) buffer (pH 8.5).

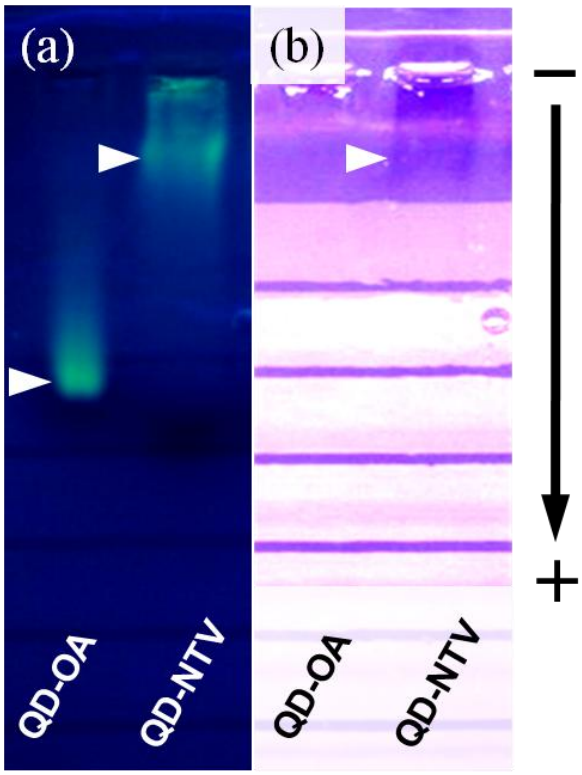

Figure 3.2. Gel electrophoresis of conjugated QDs. (a) Fluorescent images of MPA-capped QDs and NTV-conjugated QDs in 1% agarose gel after gel electrophoresis. (b) QD-NTV stained by Coomassie blue. The blue band confirms the existence of NTV proteins in QD-NTV.

Gels are run at 100 V for 80 minutes with TAE buffer as the running buffer.

Figure 3.2(a) shows the green fluorescent images of a gel plate with well-resolved separation of QD-NTV from QD-MPA. The top band in the right well is QD-NTV and the bottom band in the left well is QD-MPA only. Negatively charged QD-MPAs exhibit a reduced mobility when conjugated with the NTV, because NTV (pI 6.3) is more neutral than MPA (pKa 4.9) in TAE buffer. The same gel plate was stained with brilliant blue R (or called Coomassie blue) in the Figure 3.2(b). The interaction between SO_3^- functional group of Coomassie blue and NH_3^+ amino functional group of amino acids such as tyrosine, histidine, and phenyl alanine of Coomassie blue causes the blue stain in the protein moiety under the solution of pH 4.3. In the destaining solution (pH < 2), gel becomes transparent except the bands containing protein moieties. The blue stain of QD-NTV band confirms that there is a protein moiety in QD-NTV band. Thus, the conjugation between QD-MPA and NTV has been completed successfully. In the second way, using a Fourier Transform Infra Red (FT-IR) spectrometer, we obtained vibration spectra of functional groups of QD-MPA, NTV, and QD-NTV. The FT-IR spectra were shown in Figure 3.3. The IR bands at 1554 and 1440 cm^{-1}, at 3405 and 3350 cm^{-1}, and at 3413 cm^{-1} are characteristic bands of asymmetric and symmetric stretching bands of $–COO^–$ functional group in QD-MPA, primary amine N-H stretching bands of free NTV, and N-H stretching bands of conjugated QD-NTV, respectively (*24-25*). The amide band I and II of NTV itself are shown at 1644 cm^{-1} and at 1526 cm^{-1}. The conjugated amide bands of –CONH– functional group in QD-NTV are located 1366 cm^{-1} and 1154 cm^{-1} (red-shifted from those of QD-MPA). In the third way, we characterized and compared the hydrodynamic size of QD-MPA and QD-NTV by dynamic light scattering (DLS) analysis. The hydrodynamic size is the size of the dynamic hydrated/solvated particle measured by assuming that a particle is moving through the solution. Thus this value is more relevant parameter in a biological environment. The hydrodynamic sizes of QD-MPAs and QD-NTVs are 9.2 nm and 14.9 nm in borate buffer (pH 8.0), respectively.

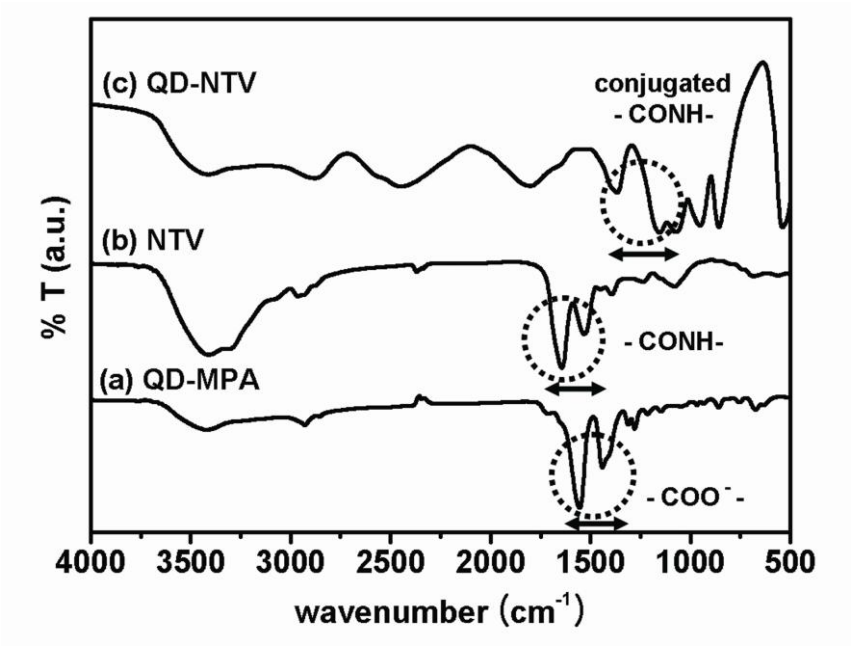

Figure 3.3. Fourier Transform Infrared (FT-IR) spectra of conjugated QDs. (a) MPA-capped QD, (b) NTV, (c) QD-NTV.

The data confirm that the hydrodynamic size of QD-NTVs is larger than that of QD-MPA due to conjugation between QD-MPA and NTV.

Next, the avidin-biotin interaction was used for the detection of TrkB receptors through ligand-receptor binding. In this study, neutravidin [MW 60 kD, pI 6.3] was chosen for the detection of TrkB receptors, because neutravidin, in contrast to streptavidin [MW 53 kD, pI 6.8-7.5] or avidin [MW 67 kD, pI 10], does not have Arg-Tyr-Asp (RYD) sequence, which may cause non-specific binding, while it has lysine-rich residues, which allows amide conjugation with carboxylic groups of QD-MPA. Additionally, since NTV as well as streptavidin is deglycosylated from avidin, oligosaccharide-based lectin binding is reduced, while biotin-binding affinity is retained (*21*). We used biotinylated anti-TrkB antibody (R&D Systems) as a binding moiety to QD-NTV. The scheme we took for fluorescence imaging was the binding via avidin-biotin coupling between TrkB receptors attached with biotinylated anti-TrkB antibodies on the neuron cells through antigen-antibody interaction and QD-NTV (a fluorescent tag).

We prepared biotinylated anti-TrkB antibody dissolved in PBS (5 μg/ml). The two-week-grown hippocampal neurons were plated at a density of 50,000 cells/cm^2 onto poly-L-lysine-coated glass bottom culture dish. Cultured hippocampal neurons were fixed with 4 % paraformaldehyde on ice for 10 min and the cells were washed with PBS more than 3 times. In order to reduce the non-specific binding, the cells were blocked with 2 % (wt/volume) of BSA dissolved in PBS for overnight at 4 ℃ and then we washed the cells with PBS more than 3 times. There are some reports that the conjugates of QDs with antibodies bind specifically to membrane receptors in both fixed and live cells *(26-28).* In the first step, we checked non-specific binding of QD-NTV to cultured primary mouse hippocampal neurons. The conjugation of QD-NTV to cultured hippocampal neurons were carried out in PBS. Mouse hippocampal neurons were incubated with 160 nM of QD-NTV for 2 hr and then we washed the cells with

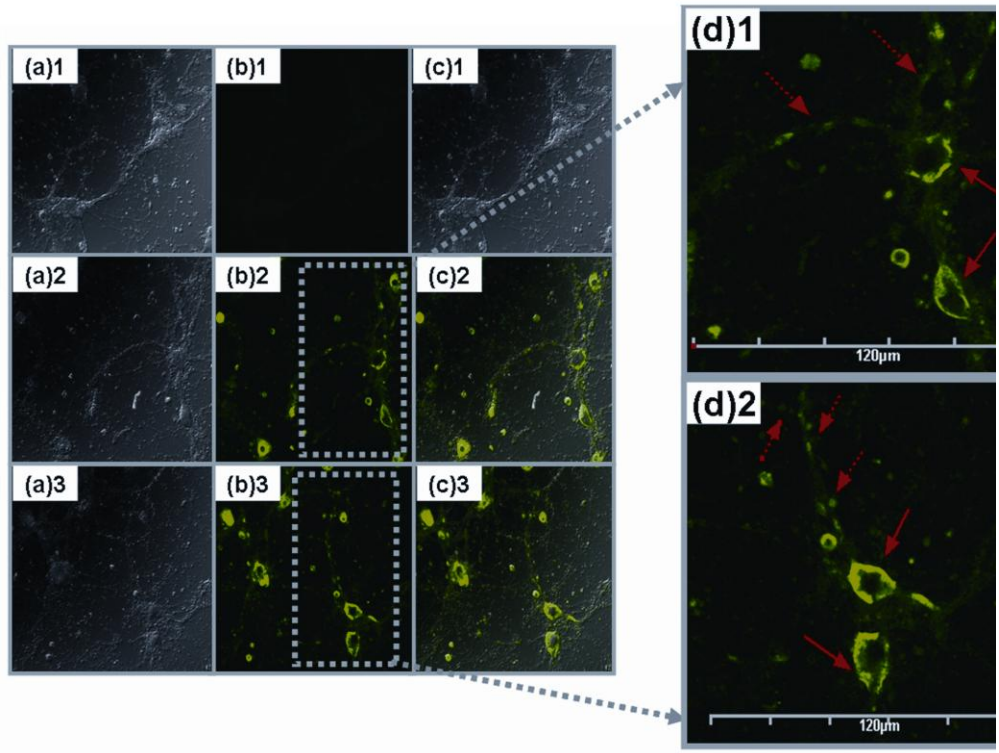

Figure 3.4. DIC and confocal fluorescence microscopic x-y images of mouse hippocampal neuron. (a) 1-2: DIC images of the neuron cell with biotinylated anti-TrkB antibody unattached and that with biotinylated anti-TrkB antibody attached, respectively. (a) 3: DIC image of other region of the neuron cell with biotinylated anti-TrkB antibody attached. (b) 1: fluorescent image of the neuron cell without any biotinylated anti-TrkB antibody treated with QD-NTV and shows no fluorescence. (b) 2-3: fluorescent images of two different regions of the cultured hippocampal neurons with biotinylated anti-TrkB antibody treated with QD-NTV. (c) 1-3: the overlapped images of (a) 1-3 and (b) 1-3, respectively. (d) 1-2: enlarged images of some part of (b) 2-3, the neuron cell bodies and neurites are marked with solid and dashed arrows, respectively.

PBS more than 3 times. After washing the cell many times, QD fluorescence signal does not appear on the surface of the cells (Fig. 3.4 (b)1). Thus, we confirm that QD-NTV rarely binds non-specifically to the cell membrane in fixed hippocampal neurons. In the second step, in order to detect endogenous TrkB receptors on the cultured hippocampal neurons, we treated the cells with biotinylated anti-TrkB antibody (5 μg/ml) dissolved in PBS buffer for 2 hr. To eliminate non-specific binding of biotinylated anti-TrkB antibody, the cells were washed with PBS several times. Biotinylated anti-TrkB antibodies were specifically located at the TrkB receptors on the neuron cells through antigen-antibody interaction. Then we incubated cultured hippocampus neurons attached with biotinylated anti-TrkB antibody with 160 nM of QD-NTV for 2 hr. QD-NTV specifically bound to biotinylated anti-TrkB antibody of the neuron cells via avidin-biotin coupling. Finally, the bioconjugation via avidin-biotin coupling between biotinylated anti-TrkB antibody located at the TrkB receptors on the neurons and QD-NTV were made for fluorescence imaging.

In Figure 3.4, (a)1-3 are DIC (differential interference contrast) images of the neuron cells. (b)1-3 are fluorescent images of the neuron cells. (c)1-3 are overlapped images of DIC images (a)1-3 with fluorescent images (b)1-3. (a)1 panel shows a DIC image of the neuron cell without any biotinylated anti-TrkB antibody treated with QD-NTV. (b)1 panel is a fluorescent image of the neuron cell without any biotinylated anti-TrkB antibody treated with QD-NTV and shows no fluorescence, and thus confirms no non-specific binding between the neuron cell and QD-NTV. Non-specifically bound QD-NTV to the cells has been eliminated through washing with PBS buffer. Figure 3.4 (a)2-3 and (b)2-3 are DIC images and fluorescent images of two different regions of the cultured hippocampus neuron cells with biotinylated anti-TrkB antibody treated with QD-NTV, respectively. QD-NTV specifically binds to biotinylated anti-TrkB antibody of the neuron cells via avidin-biotin coupling. From the overlapped images of Figure 3.4 (a)1-3 and (b)1-3 shown in (c)1-3 panels, we clearly see QD green fluorescence present

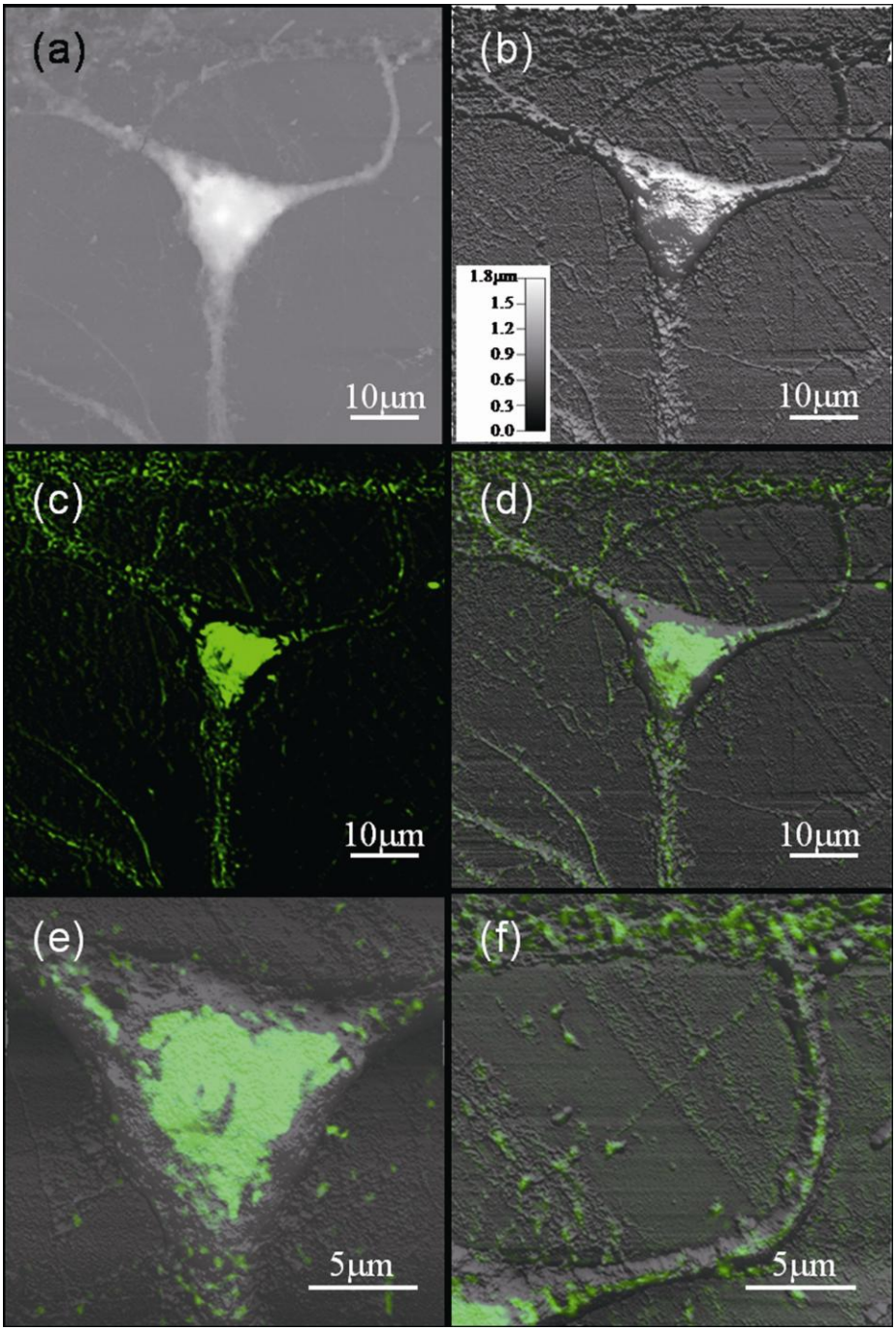

Figure 3.5. Images of the cultured hippocampal neurons acquired with combined AFM-CLSM. (a) Height contrast image. (b) 3-D surface plot of height image. (c) CLSM fluorescence image. This is two-dimensional projection fluorescence image of a 2.0 μm z-stack collected through the ×60 objective on a Fluoview 1000. (d) 3-D surface plot of height image combined with a CLSM projection image given in (c). (e) A magnified image of soma region shown in (d). (f) A magnified image of neurite region shown in (d).

on the neuron cell bodies and neurites. Figure 3.4 (c)2 and (c)3 show QD green fluorescence signals from the neuron cell bodies and neurites. More green fluorescence signal came from the neuron cell bodies. Thus, more TrkB receptors were distributed over the cell bodies (soma) than the neurites within neurons. Enlarged images of some part of Figure 3.4 (b)2-3 are shown in (d)1-2. The neuron cell bodies and neurites are marked with solid and dashed arrows, respectively. TrkB receptors in the cell bodies (soma) were distributed in a highly concentrated manner, whereas those in the neurites were distributed punctuate manner, as shown enlarged images (Fig. 3.4 (d)1-2).

With the combined AFM-CLSM, we obtained 3D images of QD-labeled TrkB receptors in hippocampal neurons and these images were shown in Figure 3.5. Prior to three-dimensional image integration, we integrated CLSM and AFM images by overlaying the 2D CLSM image, which was projected on x-y plane, on the AFM surface plots of height image to compare both images. We obtained AFM-CLSM images after dehydration and air-drying of QD-labeled neuron cells. The three-dimensional cell surface topography (Fig. 3.5 (b)) is obtained by the three-dimensional surface-plotting of the height-contrast image (Figure 3.5 (a)). The topographical image of the cell surface was shown on nanometer scale, and the cell's maximal height of ~ 1.5 μm. The 3D cellular structures, such as somata and neurites were clearly visualized. We obtained the depth-resolved (i.e., z-stack) fluorescence images of neurons in every 0.3 μm and reconstructed them (x, y, z = every 0.3 μm) to get a three-dimensional fluorescence image of neurons. The merged 3D neuron image of the structural image by AFM and the fluorescent image by CLSM is shown in Fig. 3.5 (d). Thus the whole fluorescent TrkB signals over the cell surface can be correlated to the cellular ultrastructure resolved by AFM. Magnified AFM-CLSM image shows that TrkB receptors are distributed in a highly diffuse manner in the central soma but punctate at the edge of soma (Fig. 3.5 (e)). Additionally, TrkB receptors appeared to be discrete in the neurites, and most of the TrkB receptors in the neurites were located on the high ridges of

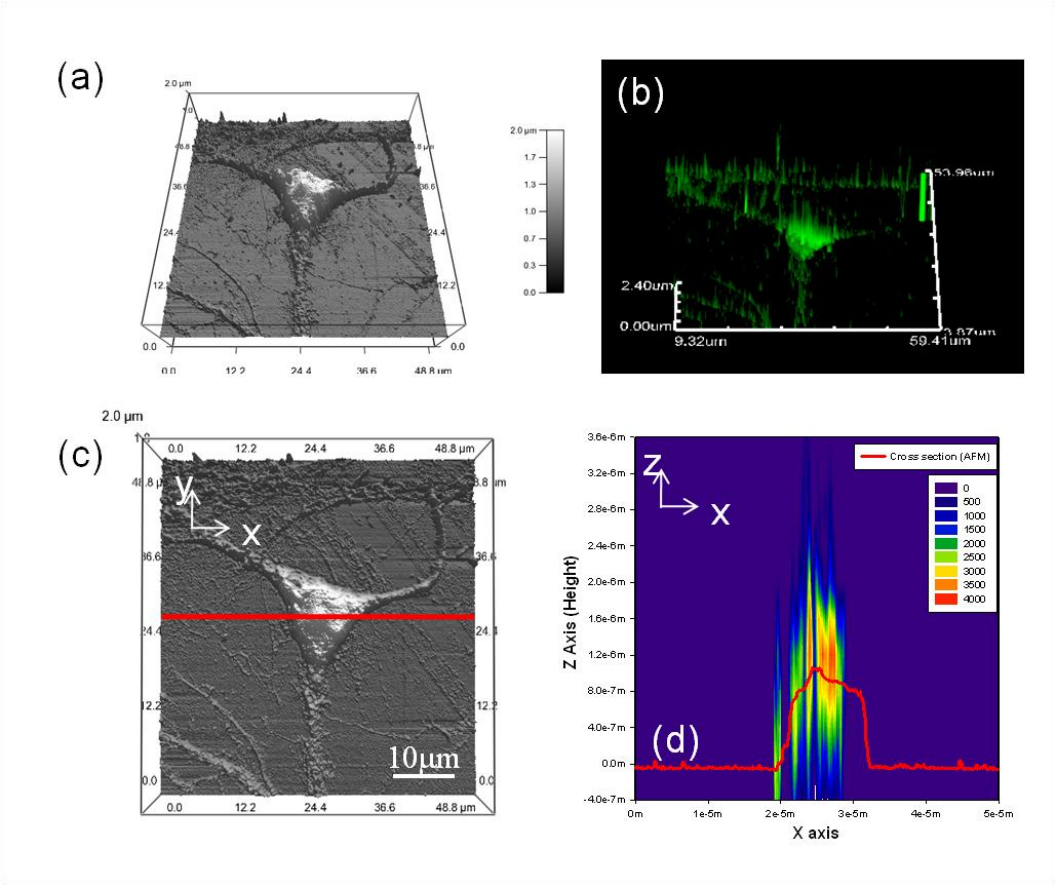

Figure 3.6. Integration of 3D AFM and 3D CLSM image. (a) Three-dimensional AFM height image, (b) Three-dimensional reconstruction of Z-stacked CLSM fluorescent image, (d) Combined AFM-CLSM image of cross-section marked in (c), showing the localization of TrkB receptor related to the structure of the cell (a view of xz plane). Red line shows cell's surface, and rainbow spectrum shows QD's fluorescent intensity. Highest intensity region indicates the QD's location, that is, TrkB receptor's location.

neurites. However, 2D CLSM – 3D AFM integrated image could provide only flat information about the distribution.

Furthermore, to determine the localization of endogenous TrkB receptors related to three-dimensional (3D) topography of the cells on nanometer-scale resolution, we integrated 3D AFM surface topography with 3D CLSM image of QD-labeled TrkB receptors in hippocampal neurons with help from the integration program using Matlab (Figure 3.6). The cross-section view of integrated 3D AFM and 3D CLSM image is shown in Fig. 3.6 (d). QD fluorescent signals were concentrated on the surface region of the cell, suggesting that the distribution pattern of TrkB receptor protein was based on the endogenous TrkB receptor protein. To date, intracellular localization of TrkB receptor protein has been previously studied by several groups. EM study with immunocytochemistry showed that TrkB receptor proteins are present in hippocampal cell bodies, axons, dendrites and dendritic spines (*11*, *13*). OM study reported that TrkB expression appeared diffuse in the soma, clustered in neuronal processed (*12*). Our results provided the distribution patterns of endogenous TrkB receptor protein not intracellular receptor protein by using the combined AFM-CLSM. Therefore, endogenous TrkB receptor proteins are distributed in a highly diffuse manner in the central soma, discrete in the neurites. Thus our AFM-CLSM analysis using QD enabled us to discover precise correlation between immunocytochemically fluorescent signals and cellular structures, which could not be done with a conventional fluorescent image analysis system.

3.5 Conclusions

We have demonstrated that the highly luminescent bioconjugates of QD-neutravidin and biotinylated anti-TrkB antibody are available to acquire the distribution

of TrkB receptors by depth-resolved fluorescent signals, which are highly correlated with nanoscale cellular structural images. We synthesized nearly monodispersed water-soluble CdSe/ZnS core/shell QDs (Q.Y. ~ 80 % at room temperature) with chemical composition gradients emitting at 520nm with a FWHM less than 30 nm. QD-NTV is made through a coupling reaction between the carboxyl group of water-soluble MPA-QD and the amino group of NTV using EDC as the coupling activator. In order to study the neurons through AFM-CLSM, we generated the bioconjugates of biotinylated anti-TrkB antibody, which detect the TrkB receptors on the surface of neurons with QD-NTV via avidin-biotin coupling. We compared the conjugated QD-NTV fluorescent signals between neurons treated with biotinylated anti-TrkB antibody and QD-NTV and neurons treated with only QD-NTV. QD fluorescence is present only on the cells treated with biotinylated anti-TrkB antibody. This result confirms the successful bioconjugation between QD-NTV and biotinylated anti-TrkB antibody. From the fluorescence study, we find that TrkB receptors are distributed broadly over the neuron cell bodies (soma), whereas they are distributed as a punctate structure on the neurites. We further discover the precise localization of TrkB receptors by correlating the fluorescent image with nanoscale cellular structures resolved by AFM. AFM-CLSM images suggest that TrkB receptors detected are but the endogenous TrkB receptor protein not the intracellular receptor protein and those are located broadly in the central soma but showing punctate structures at the edge of soma. Additionally, TrkB receptors on the neurites are located in a discrete manner on the high ridges of neurites. Over the repeated scans by AFM-CLSM imaging, the bioconjugates show no photobleaching. Thus, we suggest that our QD-based immunocytochemistry technique can be utilized for stable structural and fluorescent imaging in neurons by AFM-CLSM. Furthermore, our bioconjugate, QD-NTV-biotin-TrkB can be applied for real-time fluorescence signal trafficking or long-term imaging in live neurons.

3.6 References

(1) Xiong, Z. Q., Zheng, J., Shen, W. H., Lu, T. J., Zhou, Y., Chen, Q., Wang, Z., Xiang, T., Zhu, Y. C., Zhang, C., and Duan, S. M. (2008) Clathrin-dependent endocytosis is required for TrkB-dependent Akt-mediated neuronal protection and dendritic growth. *Journal of Biological Chemistry 283*, 13280-13288.

(2) Lohof, A. M., Ip, N. Y., and Poo, M. M. (1993) Potentiation of Developing Neuromuscular Synapses by the Neurotrophins Nt-3 and Bdnf. *Nature 363*, 350-353.

(3) Bramham, C. R., and Messaoudi, E. (2005) BDNF function in adult synaptic plasticity: The synaptic consolidation hypothesis. *Prog Neurobiol 76*, 99-125.

(4) Kang, H. J., and Schuman, E. M. (1996) A requirement for local protein synthesis in neurotrophin-induced hippocampal synaptic plasticity. *Science 273*, 1402-1406.

(5) Cheng, Q., and Yeh, H. H. (2003) Brain-derived neurotrophic factor attenuates mouse cerebellar granule cell GABA(A) receptor-mediated responses via postsynaptic mechanisms. *J Physiol-London 548*, 711-721.

(6) Levine, E. S., Dreyfus, C. F., Black, I. B., and Plummer, M. R. (1995) Brain-Derived Neurotrophic Factor Rapidly Enhances Synaptic Transmission in Hippocampal-Neurons Via Postsynaptic Tyrosine Kinase Receptors. *P Natl Acad Sci USA 92*, 8074-8077.

(7) Kang, H. J., and Schuman, E. M. (1995) Long-Lasting Neurotrophin-Induced Enhancement of Synaptic Transmission in the Adult Hippocampus. *Science 267*, 1658-1662.

(8) von Bohlen und Halbach, O., Krause, S., Medina, D., Sciarretta, C., Minichiello, L., and Unsicker, K. (2006) Regional- and age-dependent reduction in trkB receptor expression in the hippocampus is associated with altered spine

morphologies. *Biol Psychiatry 59*, 793-800.

(9) Larsson, L.-I. (1988) *Immunocytochemistry : theory and practice*, CRC Press, Boca Raton, Fla.

(10) Yan, Q., and Johnson, E. M. (1989) Immunohistochemical Localization and Biochemical-Characterization of Nerve Growth-Factor Receptor in Adult-Rat Brain. *Journal of Comparative Neurology 290*, 585-598.

(11) Yan, Q., Radeke, M. J., Matheson, C. R., Talvenheimo, J., Welcher, A. A., and Feinstein, S. C. (1997) Immunocytochemical localization of TrkB in the central nervous system of the adult rat. *Journal of Comparative Neurology 378*, 135-157.

(12) Swanwick, C. C., Harrison, M. B., and Kapur, J. (2004) Synaptic and extrasynaptic localization of brain-derived neurotrophic factor and the tyrosine kinase B receptor in cultured hippocampal neurons. *Journal of Comparative Neurology 478*, 405-417.

(13) Drake, C. T., Milner, T. A., and Patterson, S. L. (1999) Ultrastructural localization of full-length trkB immunoreactivity in rat hippocampus suggests multiple roles in modulating activity-dependent synaptic plasticity. *Journal of Neuroscience 19*, 8009-8026.

(14) Weller, H. (1993) Colloidal Semiconductor Q-Particles - Chemistry in the Transition Region between Solid-State and Molecules. *Angew Chem Int Edit 32*, 41-53.

(15) Alivisatos, A. P. (1996) Semiconductor clusters, nanocrystals, and quantum dots. *Science 271*, 933-937.

(16) Lidke, D. S., Nagy, P., Heintzmann, R., Arndt-Jovin, D. J., Post, J. N., Grecco, H. E., Jares-Erijman, E. A., and Jovin, T. M. (2004) Quantum dot ligands provide new insights into erbB/HER receptor-mediated signal transduction. *Nat Biotechnol 22*, 198-203.

(17) Michalet, X., Pinaud, F., Lacoste, T. D., Dahan, M., Bruchez, M. P., Alivisatos, A.

P., and Weiss, S. (2001) Properties of fluorescent semiconductor nanocrystals and their application to biological labeling. *Single Mol 2*, 261-276.

(18) Bruchez, M., Moronne, M., Gin, P., Weiss, S., and Alivisatos, A. P. (1998) Semiconductor nanocrystals as fluorescent biological labels. *Science 281*, 2013-2016.

(19) Chan, W. C. W., and Nie, S. M. (1998) Quantum dot bioconjugates for ultrasensitive nonisotopic detection. *Science 281*, 2016-2018.

(20) Char, K., Bae, W. K., Hur, H., and Lee, S. (2008) Single-step synthesis of quantum dots with chemical composition gradients. *Chem Mater 20*, 531-539.

(21) Mattoussi, H., Mauro, J. M., Goldman, E. R., Anderson, G. P., Sundar, V. C., Mikulec, F. V., and Bawendi, M. G. (2000) Self-assembly of CdSe-ZnS quantum dot bioconjugates using an engineered recombinant protein. *J Am Chem Soc 122*, 12142-12150.

(22) Hermanson, G. T. (1996) *Bioconjugate techniques*, Academic Press, San Diego.

(23) Banker, G., and Goslin, K. (1998) *Culturing nerve cells 2nd ed*, Vol. 2nd ed, MIT Press, Cambridge, Mass.

(24) Chen, B., Ying, Y., Zhou, Z. T., and Zhong, P. (2004) Synthesis of novel nanocrystals as fluorescent sensors for Hg2+ ions. *Chem Lett 33*, 1608-1609.

(25) Pavia, D. L., Lampman, G. M., and Kriz, G. S. (2001) *Introduction to spectroscopy : a guide for students of organic chemistry 3rd ed*, Vol. 3rd ed, Brooks/Cole ; Thomson Learning, Pacific Grove, Calif. : Australia.

(26) Vu, T. Q., and Rajan, S. S. (2006) Quantum dots monitor TrkA receptor dynamics in the interior of neural PC12 cells. *Nano Lett 6*, 2049-2059.

(27) Dahan, M., Levi, S., Luccardini, C., Rostaing, P., Riveau, B., and Triller, A. (2003) Diffusion dynamics of glycine receptors revealed by single-quantum dot tracking. *Science 302*, 442-445.

(28) Wu, X. Y., Liu, H. J., Liu, J. Q., Haley, K. N., Treadway, J. A., Larson, J. P., Ge, N. F., Peale, F., and Bruchez, M. P. (2003) Immunofluorescent labeling of cancer

marker Her2 and other cellular targets with semiconductor quantum dots (vol 21, pg 41, 2003). *Nat Biotechnol 21*, 452-452.

Chapter IV.

Volumetric changes in presynaptic structure of *Aplysia* sensory neurons during LTF

4.1 Introduction

Long-term facilitation (LTF), which has been studied as one of the major mechanisms of learning and memory in *Aplysia* nervous system, is accompanied by functional and structural changes in the synapses between sensory and motor neurons (*1-4*). Either spaced or massed application (continuous application) of 5-HT can induce the LTF (*5-7*), and the long-term increase in the synaptic strength is highly correlated with an increase in the number of functionally active varicosities when it is observed by EM and optical microscopy (*2, 8-9*). Based on these imaging techniques, it has been suggested that new varicosities are formed either by splitting of preexisting varicosities (*1-2, 10*) or by outgrowth of new filopodia (*11*). Furthermore, time-course confocal microscopy imaging technique revealed that functional activation of varicosities has two different temporal sequences: first, the rapid (3 - 6 hr) activation of preexisting empty varicosities by filling with synaptic vesicles and second, slow generation (> 24 hr) of new synaptic varicosities filled with synaptic vesicles (*2*). All the observations suggest the idea that synaptic facilitation can be supported by increase in the number of functional varicosities filled with synaptic vesicles. However, the preexisting varicosities filled with synaptic vesicles were considered relatively stable as they are always present at the fixed location throughout the induction and maintenance of LTF (*12*).

Previous EM studies have shown that varicosities in *Aplysia* sensory neurons contain numerous synaptic vesicles, microtubules, mitochondria and endoplasmic reticulum (ER) (*13-14*). Even though the size of varicosities is diverse, the concentration of synaptic vesicles inside each varicosity is relatively uniform (*13*). This observation suggests larger varicosities may contribute the larger synaptic transmission. Previous studies on LTF, however, are more focused on the numerical increase in

functional varicosities but not volumetric increase in them due to the limitations in possible imaging techniques for a three-dimensional (3D) real-time measurement of the morphological changes in preexisting functional varicosities. Thus, development of a novel technique for quantitative analyses of the fine 3D structural changes in the same synaptic varicosities during LTF is strongly required. Additionally, parallel analyses on the structural changes in synaptic varicosities and the localization of synaptic vesicles within the same varicosities are required to investigate the relationship between structural changes and functional changes during LTF.

In the present study, we have developed the combined AFM and CLSM (AFM-CLSM) instrument and investigated fine three-dimensional structural changes in synaptic connections in response to LTF-inducing stimuli within live *Aplysia* cultured neurons in addition to acquiring the three-dimensional optical images. This novel imaging system enables us to monitor detailed three-dimensional changes in the volume of varicosities and the distribution of synaptic vesicles within them in live *Aplysia* sensory neurons following 5-HT treatment. Furthermore, we concurrently analyzed the high-resolution structural and fluorescent images by using our integration program. We found that LTF-inducing stimuli increase the volume of preexisting varicosities filled with synaptic vesicles in conjunction with the increase in the total number of varicosities. Thus, we suggest that not only the number of the total varicosities but also the volume of preexisting functional varicosities are increased together to enhance the synaptic efficacy during LTF. In conclusion, using the combined AFM-CLSM, we developed a novel technique, which enables simultaneous investigation of the volumetric changes in synaptic structures and 3D intracellular mapping of synaptic vesicles in live neurons.

4.2 Experimental Section

4.2.1 Sensory-to-motor neuron coculture

Cell cultures were performed as previously described (*15-17*). Abdominal and central ganglia were dissected from *Aplysia kurodai* (50-100g) and incubated at 34 °C for 1.5 ~ 2.5 hr in 1% protease (type IX, Sigma) dissolved in isotonic L15/ASW (1:1) media (ASW: 460 mM NaCl, 10 mM KCl, 11 mM $CaCl_2$, 55 mM $MgCl_2$, and 10 mM HEPES, pH 7.6). After a thorough washing with ASW several times to remove residual protease, the ganglia were incubated at 18 ^{o}C for at least 3 hr in L15/ASW to allow recovery from heat shock. LFS motor neurons were dissected from the abdominal ganglia and cultured in a solution of 50 % *Aplysia* hemolymph in isotonic L15 media. On the next day, pleural sensory neurons were isolated from the pleural ganglia and cocultured with LFS motor neurons and maintained at 18 °C in an incubator for 3 days to allow time for the formation and stabilization of synaptic connections.

4.2.2 Microinjection of DNA constructs into *Aplysia* neurons

Microinjection into *Aplysia* neurons was performed as previously described (*18-20*). To mark active varicosities, sensory neurons in sensory-to-motor cocultures were microinjected with an injection solution containing 0.5 μg/μl of pNEX3-synaptophysin-EGFP (enhanced green fluorescent protein), 0.5 μg/μl of pNEXδ-mRFP (monomeric red fluorescent protein).

4.2.3 Long-term facilitation protocol

Cultures were exposed to 10μM 5-HT (5-hydroxytryptamine, serotonin) for 90 min as previously reported (*6*). Control cells were treated with the vehicle (L15/ASW) without 5-HT in an identical manner. To compare the changes induced by 5-HT treatment, combined AFM-CLSM images were taken 3 hr before and 24 hr after 90 min massed 5-HT treatment in the bath.

4.3 Measurements and Analysis

4.3.1 Combined AFM and CLSM

The surface structure of fluorescently labeled cells was investigated with our custom-built combined AFM-CLSM system. The fluorescence images were collected with a 20 × magnification and 0.75 NA objective lens by CLSM. In order to get a three-dimensional image, we collected the depth-resolved (z-stacked) fluorescence images of neurons in every 0.7 μm. The fluorescent image was recorded at an acquisition time of 4 ms per pixel. Right after confocal imaging, the same sample was imaged with AFM in tapping mode in liquid. After laser alignment and tip calibration, the system was left for half an hour for thermal equilibrium. The AFM probe was positioned near the varicosity not to impale the cell structure with the aid of the optical microscope. Tapping mode imaging was conducted using 60 μm-long Biolever cantilevers (Olympus, Tokyo, Japan), which had a resonance frequency of 37 kHz in air and a nominal spring constant of 0.03 N/m. The drive frequency used for imaging in liquid was set at the nominal resonance frequency of 6 ~ 8 kHz. The free-oscillation amplitude of the cantilever was set to 100 nm. The set point parameter was decreased by the smallest increment

allowing for minimal force on the sample. All AFM data were composed of 128 scan lines and 128 pixels per line and the scan speed was usually 3 μm/s. First order flattening was performed using MFP-3D image processor.

4.3.2 Quantification of the total varicosity number and the volume of varicosity

In order to count the total number of varicosities for each sensory neuron, functional varicosities were identified according to criteria previously established (*2, 9, 12-13, 21*). We considered as synaptic varicosities which had a long diameter of greater than 3 μm in contact with cell body, the axon hillock, the initial segment, and proximal processes of the motor neuron as measured by mRFP labeling. In the previous studies, these varicosities were relevant to functional synapses undergoing LTF since those varicosities had active zones. The percentage of change in varicosity number was obtained by comparing the total number of sensory neuron varicosities (5-HT-induced newly formed and preexisting) measured 24 hr after 5-HT treatment to the total number of varicosities (preexisting) measured 3hr before treatment.

In order to measure the volume of the varicosities, we analyzed 3D AFM images of them. Each pixel of AFM images is defined by its x-, y-, z- coordinates. The x- and y-coordinates are determined by the size of the scan area and the number of scan lines per image. The z- coordinate of each pixel means the height of each pixel. Thus, the volume of the varicosities can be calculated by the sum of all columns defined by x-, y-, z-coordinates. The percentage of change in varicosity volume was obtained by comparing the volume of a sensory neuron varicosity measured 24 hr after 5-HT treatment to the volume of the same varicosity measured 3 hr before treatment (*22*).

4.4 Results and Discussion

4.4.1 Concurrent functional and structural changes following 5-HT treatment

In order to analyze more accurate correlation between structural changes in synaptic varicosities and functional changes in them undergoing synaptic plasticity, we have acquired the AFM and CLSM images of the same synaptic connections before and after 5-HT treatment and simultaneously analyzed them. The 3D-integrated AFM and CLSM image implemented by Matlab routine gave us an exact correspondence of the spatial position of functional release sites marked with fluorophore within the 3D structure of synaptic varicosity related to LTF. Among the population of varicosities, we could divide it into two different populations: one is the preexisting varicosity and the other is the newly generated varicosity (*2*). First of all, AFM images provided more accurate information about the structural changes in sensory neurons and the structure of postsynaptic motor neurons, which have synaptic contacts with sensory neurons. In optical images obtained from CLSM, it seems that the new synaptic varicosity (2) was emerged next to the preexisting varicosity (1) and the preexisting varicosity remained the same size after 5-HT treatment (Fig. 4.1, 1(d) and 2(d)). However, AFM images clearly revealed that newly formed varicosity (2) was actually existed as a preexisting varicosity before 5-HT treatment, which swelled after 5-HT treatment (Fig. 4.1, 1(b), and 2(b)). Additionally, AFM images show that these two varicosities were contacting the major neurites of the motor neuron, which was not labeled with any fluorescent proteins (black arrows in Fig. 4.1, 2(a)). Additionally, optical images showed that the newly grown varicosity (2) as well as preexisting varicosity (1) were the synaptic vesicle-filled varicosities (*2*) (Fig. 4.1, 1(c) and 2(c)). Thus, they are highly relevant to

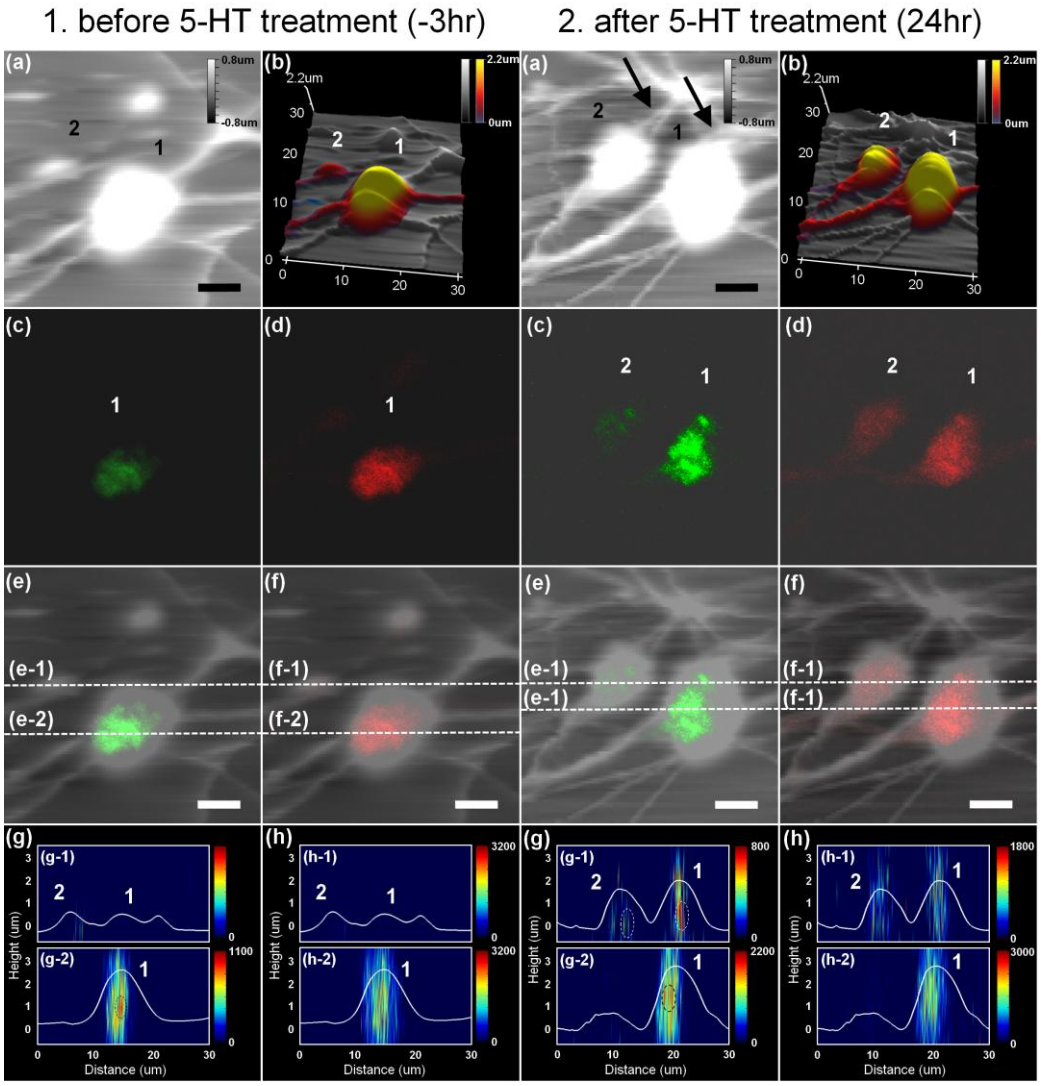

Figure 4.1. Merged AFM - CLSM images of the presynaptic change at the same synaptic area related to synaptic plasticity. (Column 1) Images obtained 3 hr before 5-HT treatment and (Column 2) 24 hr after 5-HT treatment. (a) Height contrast image obtained from AFM. (b) Three-dimensional surface plot of height image obtained from AFM. Sensory neurons among images were expressed by pseudocolor scale. (c, d) Two-dimensional fluorescent CLSM image. The sensory neuron was labeled with both synaptophysin-eGFP (c) and mRFP (d). (e, f) Height image overlaid with 2D fluorescent image of synaptophysin-eGFP (e) and mRFP (f). (g, h) Cross-section views (a view of xz plane) of the merged AFM and CLSM (3D) images marked in (e) and (f) are shown in (g) and (h), respectively, which showed the cellular distribution of synaptophysin-eGFP (dashed oval) and mRFP related to the structure of the synaptic varicosity. White lines show cell surface, and pseudocolor scale spectrums show fluorescent intensity. Scale bars, 5 μm.

functional synapses which are actively involving in synaptic transmission and undergoing synaptic plasticity during LTF. The CLSM images were overlaid on the AFM surface plots of height images (Fig. 4.1, 1(e), 1(f), 2(e), and 2(f)). The cross-section views of integrated AFM and CLSM image marked on Fig. 4.1 (1(e), 1(f), 2(e), and 2(f) are shown in Fig. 1(g), 1(h), 2(g), and 2(h), respectively). Distribution pattern of synaptophysin-eGFP and mRFP in varicosities were shown differently. Fluorescent intensities of mRFP were evenly distributed throughout both varicosities (1, 2), and were not changed by 5-HT treatment (Fig. 4.1, 1(h-2), 2(h-2)). In contrast, synaptophysin-eGFP fluorescent signals were concentrated in local regions within both varicosities (Fig. 4.1, 1(g-2), 2(g-1), and 2(g-2), dashed oval). Differences in the localization of synaptophysin-eGFP and mRFP signals are based on their cellular localization, since mRFP is diffused within cytosol whereas synaptophysin-eGFP is localized in the membrane of synaptic vesicles. The region of high-intensity synaptophysin-eGFP signal indicated the localization of concentrated synaptic vesicles. Three-dimensional distribution of synaptic vesicles was analyzed according to structural changes before and after 5-HT treatment. Synaptic vesicles were concentrated in the middle of the varicosity (1) before and after 5-HT treatment, and were partially-filled in the newly grown varicosity (2) after treatment. Although the distribution of synaptic vesicles was not altered remarkably by 5-HT treatment, we could observe three-dimensional localization of synaptic vesicles by monitoring synaptic molecules within synaptic connections in relation with synaptic morphology in live neurons. Our data support the idea that the varicosity (2) was grown from preexisting empty varicosity, and functionally activated by partially-filling with synaptic vesicles. These results indicate that the combined AFM-CLSM provided more precise insights into the movement of functional components within the changed live cell structure associated with LTF in *Aplysia* neurons. Thus, the combined AFM-CLSM is an efficient method to perform the time-course imaging of structural changes and intracellular functional

changes in live neurons.

Because changes in the morphology of synaptic varicosities have been suggested as an underlying mechanism of the maintenance of synaptic facilitation during LTF, volumetric measurement of preexisting varicosities can give more detailed idea about the correlation between LTF and the dynamic change in synaptic structures. To date, structural changes have been characterized with the alteration in the number of synaptic varicosities by two-dimensional optical imaging (*9*). Since an increase in the volume of varicosities induces an increase in fluorescent intensity of mRFP signal, the volumetric changes in the structure can be approximately quantified by the change of the total fluorescent intensity in 3D CLSM image. However, when the volumetric changes in a varicosity are compared from two consecutive days, great care is required for a proper comparison between optical intensities due to differences in the amount of expression in fluorescent proteins and the amount of CLSM exciting laser power (*9*). When the volume of varicosity in Fig. 4.1 was calculated by the sum of 3D fluorescent intensity, the volume of preexisting varicosity (1) was increased by 17.67 %. Instead, in this study, the volumetric change of presynaptic structure can be accurately measured by AFM. The volume of preexisting varicosity (1) increased by 23.3 % from 1.33×10^{-3} m^3 to 1.64×10^{-3} m^3. Although, optically imaged data showed similar tendency in increasing volumes of synaptic varicosities as measured by AFM, quantitative results showed remarkable differences between optically detected changes in fluorescent intensity and the 3D volumetric changes detected by AFM. These results might be due to relatively low resolution of CLSM image, difference in the amount of the expressed fluorescent protein on the two consecutive days and the instability of fluorescent protein. In conclusion, through the combined AFM-CLSM system, our study provided nano-scaled volumetric analysis in synaptic conjunction with the functional changes in synaptic structures of live neurons, which has been impeded in the single optical conventional microscopy.

4.4.2 Presynaptic structural changes accompanying long-term facilitation are analyzed by actual volumetric changes

In the previous studies, the presynaptic structural change associated with LTF was investigated with the changes in quantitatively measured number of presynaptic varicosities per coculture and the structural changes were observed by an optical conventional microscope (*2*, *23*). We have monitored structural changes in preexisting varicosities filled with synaptic vesicles to determine whether there was any volumetric conversion in addition to increase in the number of varicosities during LTF. This present study measured the volumetric change of the varicosities in live neurons by quantitative analysis using AFM for the first time (Fig. 4.2. – 3(a)). Synaptic varicosities of 5-HT-treated cocultures exhibited significantly greater volumetric increase than the varicosities of control cocultures. The mean volumes of varicosities in 5-HT treated cocultures were increased significantly (67.90 ± 24.94 %, $p = 0.0198$, $n = 6$, unpaired two-tailed t test), whereas that of control cocultures was decreased (-13.74 ± 15.69 %). To further ascertain that volumetric changes were related to 5-HT mediated LTF, we examined the conventional method which is counting the number of synaptic varicosities when those were imaged by AFM–CLSM system (Fig. 4.2. – 3(b)). The mean number of sensory neuron varicosities on the motor neuron 24 hr after 5-HT treatment was increased significantly (45.62 ± 12.59 %, $p = 0.0059$, unpaired two-tailed t test), whereas that of control cocultures without 5-HT treatment was decreased (-8.60 ± 9.17%). Our result correlates with the previous reports showing that the number of synaptic varicosities was significantly increased by LTF-inducing stimuli (*9*). To date, LTF-related structural changes in synaptic varicosities were mostly manifested by an alteration in the number of synaptic connections due to the limitation of techniques available for the accurate observation of the volumetric changes in the live cells. Our

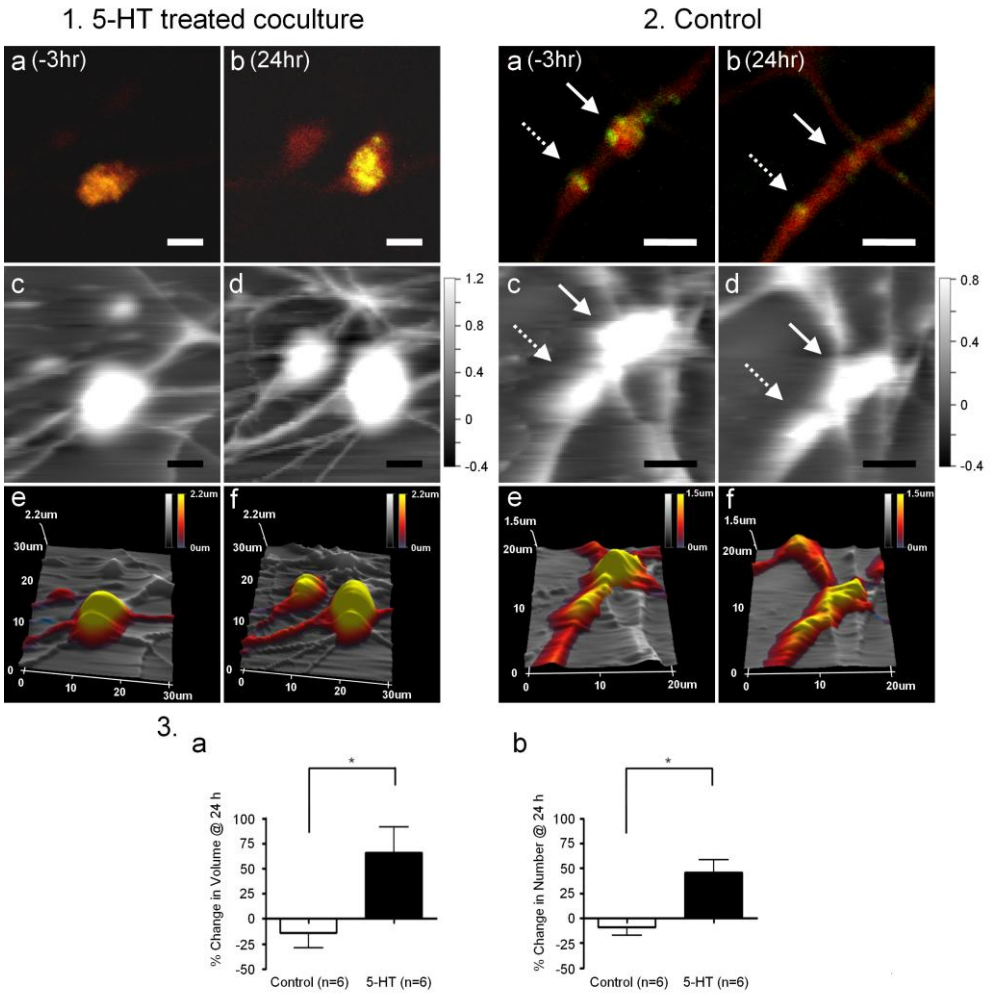

Figure 4.2. Changes in volume of synaptic varicosities and the total number of synaptic varicosities per coculture induced by 5-HT treatment characterized with combined AFM-CLSM. Images obtained in 5-HT treated condition (Column 1) and control condition (Column 2). Both synaptophysin-eGFP and mRFP were expressed in a sensory neuron among sensory-to-motor coculture prior to imaging. In column 1, synaptic varicosities were observed 3 hr before 5-HT treatment (a, c, e) and 24 hr after 5-HT treatment (b, d, f), and in column 2, the other synaptic varicosities were observed 3 hr before vehicle treatment (a, c, e) and 24 hr after vehicle treatment (b, d, f). (1a, 1b, 2a, 2b). Two-dimensional merged fluorescent images of mRFP (red) and synaptophysin-eGFP (green) indicates the localization of synaptophysin-eGFP at the synaptic varicosities (yellow). (1c, 1d, 2c, 2d) Morphological change induced by 5-HT treatment or without 5-HT treatment can be obtained by AFM height images, regardless of mRFP expression and synaptophysin-eGFP filling. Scale bar represents values in μm. (1e, 1f, 2e, 2f) Three-dimensional surface reconstruction around synaptic varicosities shown in 1c, 1d, 2c, and 2d, respectively. Sensory neurons among images were expressed by pseudocolor scale. In graph 3a, 5-HT treatment causes volumetric changes in synaptic varicosities ($^{*}p$=0.0198, unpaired two-tailed t test). In graph 3b, the total number of varicosities of the cell used in analysis of volumetric changes increased after 5-HT treatment ($^{*}p$=0.0059, unpaired two-tailed *t* test). Scale bars, 5 μm.

data showed that 5-HT treatment significantly also increases the volume of the preexisting filled varicosities, which was quantitatively proved by AFM analysis. This result provides additional support for the hypothesis that structural increase in presynaptic connections improves strength of the synaptic connection and efficiency of the synaptic transmission due to increase in synaptic area and active zone (*24-25*). Furthermore, the increased volume of synaptic varicosities may contribute to the reinforcement of the synaptic transmission by increasing the synaptic vesicle pool in them and the synaptic capacity of them. As shown in Fig. 4.2. - 1, application of 5-HT induced presynaptic modification in preexisting synapses. As the previous studies reported, the increase in the number of filled varicosities has been found in the instance of sensory synaptic varicosity (2). Sensory synaptic varicosity (2) was newly grown from the preexisting empty varicosity in contact with postsynaptic motor neuron and functionally activated by partially-filling with the synaptic vesicles labeled by synaptophysin-eGFP. Additionally, it was determined that the volumetric increase also occurred in the preexisting filled varicosity (1), which was considered structurally stable, during LTF. Thus, the volumetric conversion of preexisting filled varicosities was accompanied in addition to an increase in the number of synaptic varicosities during LTF and contributed to the increase in synaptic strength. On the contrary, without 5-HT, the preexisting synaptic varicosity in contact with the motor neuron shrunk, displaying loss of the synaptic vesicles labeled with synaptophysin-eGFP (solid and dashed arrows in Fig. 4.2 – 2(a), 2(b), 2(c) and 3(d), control coculture). In the previous studies, it was also reported that a considerable number of preexisting varicosities were eliminated without 5-HT treatment (*12*).

In conclusion, these results indicate that the combined AFM-CLSM allows us to precisely analyze the presynaptic structural changes induced by 5-HT treatment, by comparing their accurate volumetric data, and to understand these structural changes accompanying synaptic plasticity. Therefore, the structural changes in presynaptic

varicosities induced by LTF are accompanied by the volumetric increase of the preexisting filled varicosities and the increase in number of newly grown presynaptic varicosities. These structure changes improve strength of the synaptic connection and efficiency of the synaptic transmission due to an increase in active zones of synaptic areas and synaptic vesicle pools of synaptic varicosities.

4.5 Conclusions

My study provided more accurate information about the presynaptic structural and functional changes inducing long-term synaptic plasticity by the combined AFM-CLSM system. High-resolution and accurate structural information of the overall synaptic area can be acquired by AFM without any concerns of the gene expression of fluorescent proteins or instability of loaded organic dyes within the cell, which were main constrains of the optical conventional microscopy. Moreover, the structural change could be observed in live cells following temporal dynamics by AFM, which was not possible in EM. Thus, structural changes in the preexisting filled varicosities during LTF could be examined by quantitative analysis of volumetric change using AFM. Our study found that LTF accompanied by the volumetric increase of preexisting varicosities as well as the generation of new synaptic varicosities. Furthermore, we could analyze the distribution of specific proteins tagged with fluorescent proteins, such as synaptic vesicle proteins, within the 3D structure of the cell by combining CLSM to AFM.

In conclusion, these results indicate that the combined AFM and CLSM system is an efficient and suitable method to study the fine 3D structural changes in live cells and the relationship between morphological/structural changes and intracellular functional changes such as the dynamic change of synaptic connections related to synaptic plasticity. In the future, this system can be applied to monitor *in situ* structural changes

accompanying functional changes in response to instant external stimuli and provide the versatile and scalable platform to study various molecular mechanisms of neuronal functions or brain diseases.

4.6 References

(1) Bailey, C. H., and Kandel, E. R. (1993) Structural changes accompanying memory storage. *Annu Rev Physiol 55*, 397-426.

(2) Kim, J. H., Udo, H., Li, H. L., Youn, T. Y., Chen, M., Kandel, E. R., and Bailey, C. H. (2003) Presynaptic activation of silent synapses and growth of new synapses contribute to intermediate and long-term facilitation in Aplysia. *Neuron 40*, 151-65.

(3) Bailey, C. H., and Kandel, E. R. (2008) Synaptic remodeling, synaptic growth and the storage of long-term memory in Aplysia. *Essence of Memory 169*, 179-198.

(4) Bailey, C. H., Kandel, E. R., and Si, K. (2004) The persistence of long-term memory: a molecular approach to self-sustaining changes in learning-induced synaptic growth. *Neuron 44*, 49-57.

(5) Muller, U., and Carew, T. J. (1998) Serotonin induces temporally and mechanistically distinct phases of persistent PKA activity in Aplysia sensory neurons. *Neuron 21*, 1423-34.

(6) Zhang, F., Endo, S., Cleary, L. J., Eskin, A., and Byrne, J. H. (1997) Role of transforming growth factor-beta in long-term synaptic facilitation in Aplysia. *Science 275*, 1318-20.

(7) Montarolo, P. G., Goelet, P., Castellucci, V. F., Morgan, J., Kandel, E. R., and Schacher, S. (1986) A critical period for macromolecular synthesis in long-term heterosynaptic facilitation in Aplysia. *Science 234*, 1249-54.

(8) Bailey, C. H., Montarolo, P., Chen, M., Kandel, E. R., and Schacher, S. (1992) Inhibitors of protein and RNA synthesis block structural changes that accompany long-term heterosynaptic plasticity in Aplysia. *Neuron 9*, 749-58.

(9) Glanzman, D. L., Kandel, E. R., and Schacher, S. (1990) Target-dependent structural changes accompanying long-term synaptic facilitation in Aplysia neurons. *Science 249*, 799-802.

(10) Hatada, Y., Wu, F., Sun, Z. Y., Schacher, S., and Goldberg, D. J. (2000) Presynaptic morphological changes associated with long-term synaptic facilitation are triggered by actin polymerization at preexisting varicositis. *J Neurosci 20*, RC82.

(11) Udo, H., Jin, I., Kim, J. H., Li, H. L., Youn, T., Hawkins, R. D., Kandel, E. R., and Bailey, C. H. (2005) Serotonin-induced regulation of the actin network for learning-related synaptic growth requires Cdc42, N-WASP, and PAK in Aplysia sensory neurons. *Neuron 45*, 887-901.

(12) Miniaci, M. C., Kim, J. H., Puthanveettil, S. V., Si, K., Zhu, H., Kandel, E. R., and Bailey, C. H. (2008) Sustained CPEB-dependent local protein synthesis is required to stabilize synaptic growth for persistence of long-term facilitation in Aplysia. *Neuron 59*, 1024-36.

(13) Bailey, C. H., Thompson, E. B., Castellucci, V. F., and Kandel, E. R. (1979) Ultrastructure of the synapses of sensory neurons that mediate the gill-withdrawal reflex in Aplysia. *J Neurocytol 8*, 415-44.

(14) Malkinson, G., Fridman, Z. M., Kamber, D., Dormann, A., Shapira, E., and Spira, M. E. (2006) Calcium-induced exocytosis from actomyosin-driven, motile varicosities formed by dynamic clusters of organelles. *Brain Cell Biol 35*, 57-73.

(15) Schacher, S., and Proshansky, E. (1983) Neurite regeneration by Aplysia neurons in dissociated cell culture: modulation by Aplysia hemolymph and the presence of the initial axonal segment. *J Neurosci 3*, 2403-13.

(16) Lee, J. A., Kim, H. K., Kim, K. H., Han, J. H., Lee, Y. S., Lim, C. S., Chang, D. J., Kubo, T., and Kaang, B. K. (2001) Overexpression of and RNA interference with the CCAAT enhancer-binding protein on long-term facilitation of Aplysia sensory to motor synapses. *Learn Mem 8*, 220-6.

(17) Lee, J. A., Kim, H., Lee, Y. S., and Kaang, B. K. (2003) Overexpression and RNA interference of Ap-cyclic AMP-response element binding protein-2, a repressor of long-term facilitation, in Aplysia kurodai sensory-to-motor synapses. *Neurosci Lett 337*, 9-12.

(18) Kaang, B. K. (1996) Neuronal expression of reporter genes in the intact nervous system of Aplysia. *Molecules and Cells 6*, 285-295.

(19) Kaang, B. K. (1996) Parameters influencing ectopic gene expression in Aplysia neurons. *Neurosci Lett 221*, 29-32.

(20) Kaang, B. K., Pfaffinger, P. J., Grant, S. G., Kandel, E. R., and Furukawa, Y. (1992) Overexpression of an Aplysia shaker K+ channel gene modifies the electrical properties and synaptic efficacy of identified Aplysia neurons. *Proc Natl Acad Sci U S A 89*, 1133-7.

(21) Glanzman, D. L., Kandel, E. R., and Schacher, S. (1989) Identified target motor neuron regulates neurite outgrowth and synapse formation of aplysia sensory neurons in vitro. *Neuron 3*, 441-50.

(22) Schneider, S. W., Pagel, P., Rotsch, C., Danker, T., Oberleithner, H., Radmacher, M., and Schwab, A. (2000) Volume dynamics in migrating epithelial cells measured with atomic force microscopy. *Pflugers Arch 439*, 297-303.

(23) Bailey, C. H., and Chen, M. (1988) Long-term memory in Aplysia modulates the total number of varicosities of single identified sensory neurons. *Proc Natl Acad Sci U S A 85*, 2373-7.

(24) Bailey, C. H., and Chen, M. (1988) Long-Term Sensitization in Aplysia Increases the Number of Presynaptic Contacts onto the Identified Gill Motor Neuron L7. *P Natl Acad Sci USA 85*, 9356-9359.

(25) Bailey, C. H., and Chen, M. (1983) Morphological basis of long-term habituation and sensitization in Aplysia. *Science 220*, 91-3.

Appendix

Appendix 1. Matlab script for 3D integration of AFM and CLSM images

m-file (1)

```
% Matlab ver.7.0.4
% Matlab script for Fig. 2.9 (F-1)
% afm.txt is z coordinates of each point from AFM data.
% clsm.txt is the values of fluorescent intensity of every.
% Channel means the values of fluorescent intensity obtained from the each focal plane.
close all;
clear all;

load afm.txt;
load clsmg.txt
value=clsmg;

z=afm;
ztemp=afm;
%z=fliplr(afm);
z=rot90(z);
ztemp=rot90(ztemp);
%%%
```

```
%%%%%%%%%%%%%%%%%%%%%%%%%%    channel 3
k=1;
for i=1:152
    for j=1:152
        ch3(i,j)=value(k,3);
        k=k+1;
    end
end

%%%%%%%%%%%%%%%%%%%%%%%%%%    channel 4
k=1;
for i=1:152
    for j=1:152
        ch4(i,j)=value(k,4);
        k=k+1;
    end
end

%%%%%%%%%%%%%%%%%%%%%%%%%%    channel 5
k=1;
for i=1:152
    for j=1:152
        ch5(i,j)=value(k,5);
        k=k+1;
    end
end


%%%%%%%%%%%%%%%%%%%%%%%%%%    channel 6
k=1;
for i=1:152
    for j=1:152
        ch6(i,j)=value(k,6);
        k=k+1;
    end
end

%%%%%%%%%%%%%%%%%%%%%%%%%%    channel 7
k=1;
for i=1:152
    for j=1:152
        ch7(i,j)=value(k,7);
        k=k+1;
    end
end

%%%%%%%%%%%%%%%%%%%%%%%%%%    channel 8
k=1;
for i=1:152
    for j=1:152
        ch8(i,j)=value(k,8);
        k=k+1;
    end
end

%%%%%%%%%%%%%%%%%%%%%%%%%%    channel 9
k=1;
for i=1:152
    for j=1:152
        ch9(i,j)=value(k,9);
        k=k+1;
    end
end
```

```
%%%%%%%%%%%%%%%%%%%%%%%%%%    channel 10
k=1;
for i=1:152
    for j=1:152
        ch10(i,j)=value(k,10);
        k=k+1;
    end
end

%%%%%%%%%%%%%%%%%%%%%%%%%%    channel 11
k=1;
for i=1:152
    for j=1:152
        ch11(i,j)=value(k,11);
        k=k+1;
    end
end

%%%%%%%%%%%%%%%%%%%%%%%%%%    channel 12
k=1;
for i=1:152
    for j=1:152
        ch12(i,j)=value(k,12);
        k=k+1;
    end
end

%%%%%%%%%%%%%%%%%%%%%%%%%%    channel 13
k=1;
for i=1:152
    for j=1:152
        ch13(i,j)=value(k,13);
        k=k+1;
    end
end

%%%%%%%%%%%%%%%%%%%%%%%%%%    channel 14
k=1;
for i=1:152
    for j=1:152
        ch14(i,j)=value(k,14);
        k=k+1;
    end
end

%%%%%%%%%%%%%%%%%%%%%%%%%%    channel 15
k=1;
for i=1:152
    for j=1:152
        ch15(i,j)=value(k,15);
        k=k+1;
    end
end

%%%%%%%%%%%%%%%%%%%%%%%%%%    channel 16
k=1;
for i=1:152
    for j=1:152
        ch16(i,j)=value(k,16);
        k=k+1;
    end
end
```

```
%%%%%%%%%%%%%%%%%%%%%%%%%%    channel 17
k=1;
for i=1:152
      for j=1:152
            ch17(i,j)=value(k,17);
            k=k+1;
      end
end

  y=-4.2:0.7:7.0;
x=1:(500/152):500;

%zzi=zzi+2.0e-7;

zzi=zzi*1.0e006;
```

m-file (2)

```
%cho=2
%ii=250

ii1=ii;
ii1=round(ii1*152/500);
figure(1)
if cho==1

      x1(17,:)=ch1(ii1,:);
      x1(16,:)=ch2(ii1,:);
      x1(15,:)=ch3(ii1,:);
      x1(14,:)=ch4(ii1,:);
      x1(13,:)=ch5(ii1,:);
      x1(12,:)=ch6(ii1,:);
      x1(11,:)=ch7(ii1,:);
      x1(10,:)=ch8(ii1,:);
      x1(9,:)=ch9(ii1,:);
      x1(8,:)=ch10(ii1,:);
      x1(7,:)=ch11(ii1,:);
      x1(6,:)=ch12(ii1,:);
      x1(5,:)=ch13(ii1,:);
      x1(4,:)=ch14(ii1,:);
      x1(3,:)=ch15(ii1,:);
      x1(2,:)=ch16(ii1,:);
      x1(1,:)=ch17(ii1,:);

      plot(x,zzi(ii1,:),'m','LineWidth',2)
      title(['Xaxis ',num2str(ii)]);
      hold on
end

if cho==2

      x1(17,:)=ch1(:,ii1);
      x1(16,:)=ch2(:,ii1);
      x1(15,:)=ch3(:,ii1);
      x1(14,:)=ch4(:,ii1);
      x1(13,:)=ch5(:,ii1);
      x1(12,:)=ch6(:,ii1);
      x1(11,:)=ch7(:,ii1);
      x1(10,:)=ch8(:,ii1);
      x1(9,:)=ch9(:,ii1);
      x1(8,:)=ch10(:,ii1);
```

```
        x1(7,:)=ch11(:,ii1);
        x1(6,:)=ch12(:,ii1);
        x1(5,:)=ch13(:,ii1);
        x1(4,:)=ch14(:,ii1);
        x1(3,:)=ch15(:,ii1);
        x1(2,:)=ch16(:,ii1);
        x1(1,:)=ch17(:,ii1);

        plot(x,zzi(:,ii1),'m','LineWidth',2)
%       plot(x,zzi(:,ii))
        title(['YAxis ',num2str(ii)]);
        hold on
end

% Output the CLSM image of each focal plane
pcolor(x,y,x1)
%image(x,y,x1)
shading interp

xlabel('μm');
ylabel('μm');

xlim([0 500])
ylim([-4.2 7.0])

hold off
```

국문초록

본 학위 논문에서는 원자간 힘 현미경-공초점 레이저 주사 현미경 통합기기 (Combined AFM-CLSM system)의 개발 및 이를 이용하여 학습과 기억의 기작을 밝히는 연구에 응용하였다. 개발된 통합기기는 살아있는 세포의 고해상도 3차원 구조 변화를 연구하는데 적합하며, 신경계의 기작이나 현상과 관련된 시냅스의 구조 변화와 구조내부의 기능 변화의 관계를 함께 연구하는데도 적합하다.

Brain-derived neurotrophic factor (BDNF)는 시냅스의 신호전달과 시냅스 가소성을 조절하는 중요한 neurotrophin 중의 하나이다. 다양한 BDNF 의 기능들은 티로신 B 키나아제 수용체 (Tyrosine kinase B receptor)를 통해 조절된다. 우리는 양자점을 기반으로 한 면역세포화학 (immunocytochemistry)를 이용하여 티로신 B 키나아제 수용체의 위치를 감지하였다. 통합기기를 이용하여 쥐의 해마세포 내부에서, 기능을 위해 세포막 표면에 위치하고 있는 endogenous 티로신 B 키나아제 수용체의 위치를 측정하였다. 이로써 endogenous 티로신 B 키나아제 수용체는 해마세포의 몸 부위의 표면에는 전체적으로 존재하고 신경돌기 부위에는 반점 형태로 존재한다는 것을 알아내었다.

애플리시아 (*Aplysia*)의 감각뉴론 (sensory neuron) - 운동뉴론 (motor neuron) 공동배양의 구조 및 기능의 가소성 (plasticity)은 학습과 기억의 기작을 이해하기 위해 많이 연구되어 왔다. 애플리시아의 장기기억 (long-term memory)의 잘 알려진 세포 모델인 시냅스의 장기 강화 (long-term facilitation)는 새로운 시냅스의 성장을 동반하게 된다. 우리는 이제까지 안정하다고 여겨진 전시냅스 구조 (varicosity)의 구조변화를 정확한 부피변화 측정을 통해 관찰하였다. 세로토닌 처리로 장기강화를 유도하였을 때, 새로운 시냅스의 성장에 의한 시냅스의 수 증가뿐 아니라, 시냅스 소낭이 채워져 있는 전시냅스 구조가 부피 증가의 변화를 일으킨다는 것을 알아내었다. 이러한 결과는 결국 장기기억을 위한 시냅스의 장기강화를 위해, 시냅스 수의 증가뿐 아니라, 기존 시냅스의 부피 변화를 통해 시냅스 내부의 시냅스 소낭의 수를 증가시켜 시냅스 신경전달 (synaptic transmission)이 용이하도록 변화한다는 것을 의미한다. 이러한 결과들은 개발된 통합기기가 면역세포화학적으로 표지된 단백질의 위치를 세포의 3 차원 구조와 연관 지어 밝혀내고, 살아있는 신경세포의 시냅스의 구조변화와 기능변화를 연관 지어 동시에 관찰하는 것이 관찰하는 것이 가능하다는 것을 보인다.

주요어: 원자간 힘 현미경, 공초점 레이저 주사 현미경, 시냅스 가소성, 장기 강화

감사의 글

이 논문이 나오기까지 나를 단련시키고, 지키시고,
인도하신 하나님께 모든 영광과 감사를 드립니다.